Alma Mater Studiorum · Università di Bologna

Dipartimento di Fisica e Astronomia "Augusto Righi"
Corso di Laurea in Fisica

Ab initio study of the electronic structure and optical properties of the Au(111) surface

Relatrice:
Prof. Margherita Marsili

Presentata da:
Ilaria Core

Anno Accademico 2025/2026

Solo dopo aver conosciuto la superficie delle cose
ci si può spingere a cercare quel che c'è sotto.
Ma la superficie delle cose è inesauribile.
Italo Calvino, *Palomar*

Contents

Sommario

Il presente lavoro di tesi analizza attraverso calcoli da principi primi la struttura elettronica e le proprietà ottiche della superficie (111) dell'oro. Lo scopo di questo studio è quello di contribuire all'individuazione del sistema minimale per ottenere simulazioni accurate della formazione di adatomi indotta dalla luce sulla superficie d'oro, mediante la teoria del funzionale densità.

I calcoli relativi alla struttura elettronica sono stati svolti tramite codici provenienti dalla suite Quantum ESPRESSO (impiegando pseudopotenziali *norm-conserving* e il funzionale PBE), mentre gli spettri di assorbimento sono stati ottenuti mediante il codice YAMBO.

In seguito a una caratterizzazione esaustiva della struttura elettronica e degli spettri di assorbimento dell'oro bulk, per modellizzare la superficie (111) dell'oro sono state generate delle slab con spessore variabile tra 2 e 10 strati atomici. Ne è stata calcolata la densità degli stati, proiettata poi sugli orbitali atomici 5d e risolta per strato. L'analisi comparata della PDOS risolta sugli strati atomici mostra che lo strato centrale della slab con cinque strati tende a riprodurre il profilo del bulk; si suggerisce dunque l'impiego della slab da cinque strati atomici come modello minimale per la superficie d'oro su cui si osserva la formazione degli adatomi. Gli spettri di assorbimento della slab si avvicinano al profilo del bulk al di sopra della soglia delle transizioni interbanda, mentre a energie inferiori emergono picchi che dipendono dallo spessore della slab.

Abstract

The present thesis investigates the electronic structure and optical properties of the Au(111) surface through *ab initio* calculations. The aim of this study is to contribute to the identification of the minimal system for accurate density functional theory simulations of the light-activated adatom formation at gold surfaces.

Electronic structure calculations are performed with codes from the Quantum ESPRESSO suite (employing norm-conserving pseudopotentials and the PBE functional), while optical absorption spectra within the random phase approximation are computed using the YAMBO code.

After a comprehensive characterization of the electronic structure and optical absorption spectra for bulk gold, Au(111) slabs of thickness varying between 2 and 10 atomic layers are constructed. Their density of states is evaluated, then projected onto the 5d atomic orbitals and layer-resolved. The comparative analysis of the layer-resolved PDOS shows that the central layer of the 5-layer slab begins to approximate the bulk profile; the 5-layer Au(111) slab is thus suggested as minimal model of the gold facet involved in light-induced adatom formation. The optical absorption spectra of the slabs approach the bulk profile above the interband threshold, while thickness-dependent peaks emerge at lower energies.

Introduction

This thesis is positioned within the broader context of a study aimed at deepening the comprehension of a peculiar phenomenon: the extraction of individual atoms from a gold facet, with molecules in its vicinity, through light irradiation of only a few microwatts. Lin et al. investigated this process in a 2022 study[1]. Their work focused on systems composed of a gold nanoparticle placed on a gold mirror, with a self-assembled monolayer placed in between; monolayers of three different molecular species were considered (biphenyl-4-thiol, 4-mercaptobenzonitrile and 4-mercaptopyridine). These systems are presented in Fig.(1). It was found that, if the nanocavity constructed by such systems is irradiated with a laser, the plasmonic field is localized to picometer scales, yielding single-molecule vibrational spectra; in other words, picocavities are formed. Picocavities originate from single-atom protrusions on metallic surfaces, as illustrated in Fig.(1): this means that illumination causes individual atoms to be pulled out of the gold nanoparticle facet. Millions of spectra obtained through surface-enhanced Raman spectroscopy (SERS) were analyzed. It was found that at low laser power no picocavities are observed, as shown in Fig.(1); their formation rate then rises slowly with laser intensity, as shown in Fig.(2), and increases abruptly above a certain threshold. This threshold was found to be significantly dependent on the molecular species forming the self-assembled monolayer, just as the characteristic lifetimes of the picocavities -which can extend to minutes for MPy, as documented in Fig.(2). The fact that picocavities are not observed at the lowest laser powers suggested that the extraction of single gold adatoms is triggered by illumination. The formation of an adatom cannot be due only to thermal effects: the gold surface was kept at room temperature and overcoming the adatom formation barrier $U_f \sim 1$ eV by simple thermal fluctuations would require a temperature above 12,000 K. Consequently, in order to explain the results, the authors proposed a novel "optical plucking" model, in which an irradiated gold atom on the surface acts as a dipole, which in turn generates a local field that polarizes the nearest molecule tip. An attractive optical force between the gold atom and the molecule arises and the attracted molecule is drawn closer to the nanoparticle facet, reducing the energy barrier for adatom formation. The barrier height decreases with growing laser intensity, until, at the intensity threshold, the barrier becomes low enough that the gold atom can be plucked out of the nanoparticle surface by thermal fluctuations at room temperature. The refinement

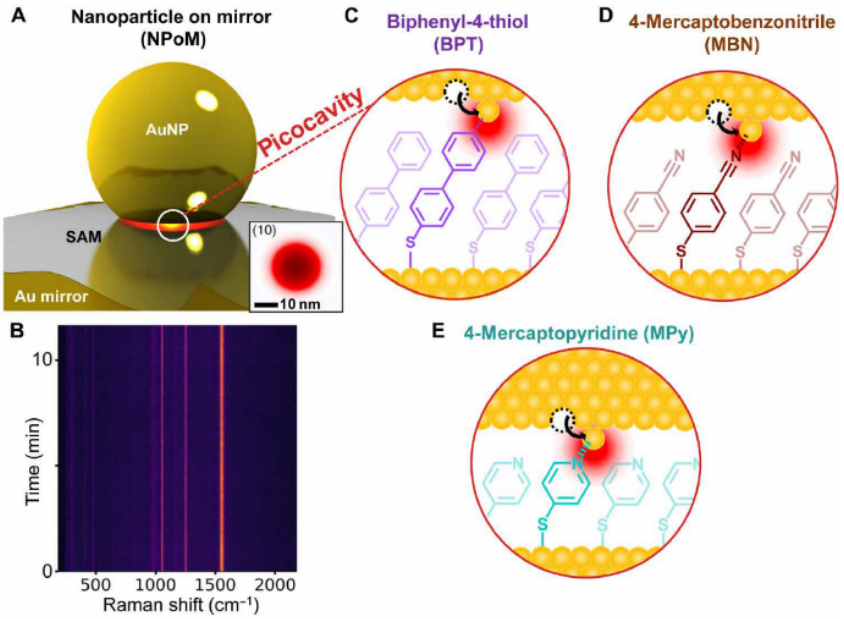

Figure 1: Au nanoparticle-on-mirror (NPoM) configuration and picocavity formation (A) Schematic illustration of Au NPoM configuration, with a self-assembled monolayer (SAM) of BPT (purple), MBN (brown), or MPy (cyan) sandwiched in the gap. The inset shows the optical field distribution at plasmon resonance, confined within the nanocavity. (B) SERS spectra acquired every 100 ms from a BPT NPoM at 20 μW: no picocavities are visible at this low excitation power. (C to E) Picocavities arising from the formation of a single gold adatom at the nanoparticle facet. Image source: Lin, Qianqi, et al. "Optical suppression of energy barriers in single molecule-metal binding." *Science advances* 8.25 (2022): eabp9285.

of the optical plucking model would represent a step forward in the comprehension of interactions between molecules and metallic surfaces, crucial in catalysis, bio/molecular sensing, molecular electronics, and electrochemistry. Moreover, the understanding of the opto-molecular mechanisms that lead to the rearrangement of metallic interfaces could enable the control of reactions at the single-atom level, which could be applicable to the development of quantum and optoelectronic devices.

Density functional theory (DFT) simulations represent a powerful tool to study this phenomen. However, simulating a system composed of a gold nanoparticle on a gold mirror with a self-assembled monolayer in the constructed plasmonic gap, irradiated by light, involves a significant computational cost; as a consequence, determining the minimal system that accurately reproduces the experimental results is of fundamental importance.

The purpose of the present thesis is to contribute to the identification of the minimal system by studying through DFT simulations the electronic structure and the optical

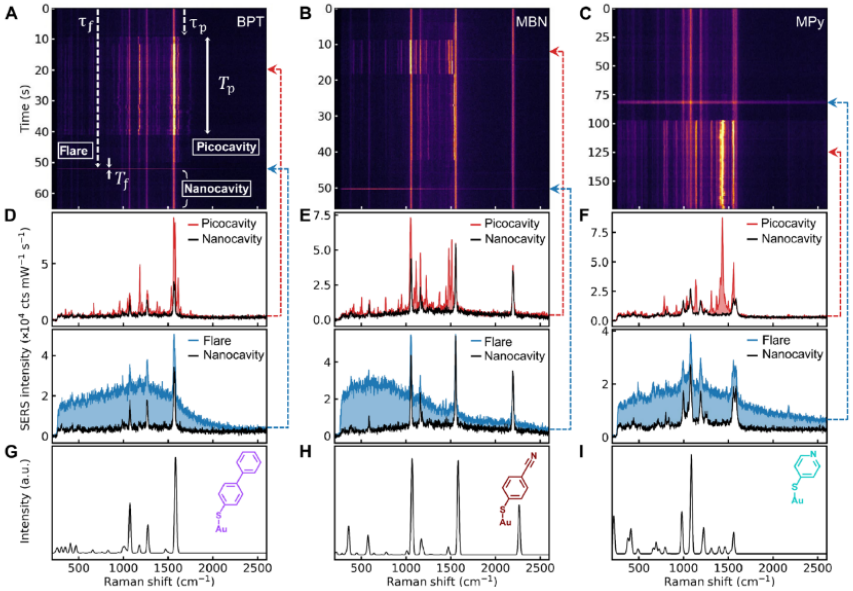

Figure 2: SERS time evolution of picocavities and flares and DFT calculated spectra (A) Time-series SERS spectra of BPT under 50-μW, 633-nm laser irradiation. The spectra from the nanocavity, the picocavity and the flare are shown. τ_p and T_p respectively indicate the formation time and lifetime of a picocavity; τ_f and T_f are the corresponding quantities for flares. (B) and (C) Analogous time series for MBN (50 μW) and MPy (10 μW). (D to F) Representative SERS spectra from a nanocavity (black), a picocavity (red), and a flare (blue). (G to I) DFT-calculated Raman spectra of BPT, MBN, and MPy. Image source: Lin, Qianqi, et al. "Optical suppression of energy barriers in single molecule-metal binding." *Science advances* 8.25 (2022): eabp9285.

properties of the Au(111) surface through slabs of different thickness. The thesis is organized as follows. Chapter 1 is devoted to the presentation of the theoretical framework of density functional theory (DFT), along with the computational methods required for its implementation in electronic-structure and optical-properties calculations for crystalline solids. Chapter 2 is centered on the presentation and analysis of the attained results of DFT electronic-structure and optical-properties simulations, performed on bulk Au and Au(111) slabs of varying thickness. The band structure, density of states and projected density of states of bulk gold are computed in the scalar-relativistic and in the fully-relativistic regime; subsequently, the optical absorption spectrum in the long-wavelength limit of bulk gold is computed in the random phase approximation, both at the independent-particle level and including local field effects. A calculation of the density of states and layer-projected density of states for the Au(111) slabs is performed. Finally, the optical absorption spectrum in the long-wavelength limit is computed for the Au(111) slabs composed of 2, 5 and 10 atomic layers; the random phase approximation

is employed, both disregarding and including local field effects. The conclusive Chapter 3 reports and summarizes the main results of the present study, addresses its limitations and outlines possible future developments.

Chapter 1

Methods

In this chapter, the theoretical framework of this thesis is discussed, along with the computational methods required for its implementation in electronic-structure and optical-properties calculations; particular attention is devoted to crystalline solids. Initially, generalities on the many-body problem are presented and the Born-Oppenheimer approximation is introduced. Moreover, key concepts in the theory of periodic solids are explained. Subsequently, density functional theory, the most widespread method to carry out ab initio calculations of the ground-state properties of many-body systems, is described in its exact formulation. The main numerical approximations and techniques required in DFT calculations are also pointed out. Finally, time-dependent density functional theory is presented and an expression for the macroscopic dielectric function of a solid is derived through the TDDFT formalism in the linear response regime.

1.1 The many-body problem

The systems of interest in condensed matter physics -such as atoms, molecules and solids- are composed of mutually interacting electrons and nuclei[2]. The total non-relativistic Hamiltonian of a system composed of N electrons (of coordinates $\mathbf{r}_i$, mass m_e, and charge $-e$) and M nuclei (of coordinates $\mathbf{R}_I$, masses M_I, and charge $+Z_I e$), is

$$\hat{H} = -\frac{\hbar^2}{2m_e}\sum_i \nabla_i^2 - \sum_I \frac{\hbar^2}{2M_I}\nabla_I^2 + \sum_i V_{nucl}(\mathbf{r}_i) + \frac{1}{2}\sum_{i\neq j}\frac{e^2}{|\mathbf{r}_i - \mathbf{r}_j|} + \frac{1}{2}\sum_{I\neq J}\frac{Z_I Z_J e^2}{|\mathbf{R}_I - \mathbf{R}_J|}, \quad (1.1)$$

where

$$V_{nucl}(\mathbf{r}) = -\sum_I \frac{Z_I e^2}{|\mathbf{r} - \mathbf{R}_I|}. \quad (1.2)$$

The terms in Eq.(1.1) represent, respectively, the kinetic energy of the electrons, the kinetic energy of the nuclei, and the potential energy associated with the nucleus-electron, electron-electron, and nucleus-nucleus Coulomb interactions. The coupling between charged particles in this Hamiltonian therefore arises from instantaneous, spin-independent Coulomb interactions. The stationary states of the system are given by the time-independent many-body Schrödinger equation, which consists of the eigenvalue relation

$$\hat{H}\Psi(\mathbf{r}_1, ..., \mathbf{r}_N, \mathbf{R}_1, ..., \mathbf{R}_M) = E_{TOT}\Psi(\mathbf{r}_1, ..., \mathbf{r}_N, \mathbf{R}_1, ..., \mathbf{R}_M) \tag{1.3}$$

In practice, due to the dependence of Eq.(1.3) on the coordinates of N+M particles, computing the exact solution to this coupled problem is unfeasible for systems consisting of a large number of particles. Consequently, it is necessary to introduce approximations to obtain a simpler form for the Schrödinger equation.

1.2 The Born-Oppenheimer approximation

A useful approximation to solve the many-body Schrödinger equation, which allows one to decouple the dynamics of the electrons from the dynamics of the nuclei, is suggested by the large difference between electron and nuclear masses[2]. The mass of a single proton is approximately 1836 times greater than the mass of an electron[3]: the nuclei are thus significantly more massive than the electrons. The Born-Oppenheimer (or adiabatic) approximation consists in setting the nuclear masses M_I to infinity and, as a consequence, neglecting the kinetic energy of the nuclei. In this framework, the position coordinates of the nuclei $\mathbf{R}_I$ serve as parameters in the many-body Hamiltonian and the nuclei are considered fixed in a selected configuration. The term representing the repulsive interaction between nuclei is therefore a constant. It contributes to the total energy of the system; it can be ignored while studying the electronic states, but, of course, it contributes when forces are evaluated. The Hamiltonian of a system of N interacting electrons in the presence of nuclei fixed in a given configuration is

$$\hat{H}_e = \hat{T} + \hat{V}_{int} + \hat{V}_{ext}, \tag{1.4}$$

where the terms respectively represent the kinetic energy of the electrons, the potential due to the electron-electron Coulomb interaction and the potential acting on the electrons due to the nuclei[4]. Hartree atomic units ($\hbar = e = m_e = 4\pi/\epsilon_0 = 1$) are used throughout. The terms in Eq.(1.4) can be written as

$$\hat{T} = -\sum_i \frac{\nabla_i^2}{2} \tag{1.5}$$

$$\hat{V}_{int} = \frac{1}{2}\sum_{i \neq j} \frac{1}{|\mathbf{r}_i - \mathbf{r}_j|} \tag{1.6}$$

$$\hat{V}_{ext} = \sum_i V_{ext}(\mathbf{r}_i) = -\sum_{i,I} \frac{Z_I}{|\mathbf{r}_i - \mathbf{R}_I|}. \tag{1.7}$$

The effect of the nuclei on the electrons in the electronic Hamiltonian $\hat{H}_e$ is incorporated into the "external" potential expressed by the operator $\hat{V}_{ext}$ in Eq.(1.7). The time-independent Schrödinger equation for the system of N interacting electrons becomes

$$\hat{H}_e \Psi(\mathbf{x}_1, ..., \mathbf{x}_N) = E\Psi(\mathbf{x}_1, ..., \mathbf{x}_N), \tag{1.8}$$

where $\mathbf{x}_i = \mathbf{r}_i\sigma_i$ denotes the spatial and spin coordinates of the i-th electron. The wavefunction Ψ must be antisymmetric with respect to the exchange of the variables $\mathbf{x}_i$. The eigenvalue problem in Eq.(1.8) depends only parametrically on the nuclear positions $\mathbf{R}_I$; however, it remains impossible to solve exactly for a large number of electrons. Indeed, the Coulomb interaction potential $\hat{V}_{int}$ couples the degrees of freedom of the electrons, and Ψ depends on 3N position variables. For this reason, further levels of approximation and different strategies are required.

1.3 Crystalline solids: band structure and density of states

The physical description of most solid-state systems, whether metallic or insulating, relies on the understanding of the fundamental properties of periodic arrays. The properties of periodic lattices and how they influence the electronic structure of a solid are detailed below.

The Bravais lattice and the reciprocal lattice

The periodic structure of a crystalline solid is described through its Bravais lattice, which specifies the arrangement of the repeated units of the crystal. A Bravais lattice formally consists in all points with position vectors $\mathbf{R}$ in the form $\mathbf{R} = n_1\mathbf{a}_1 + n_2\mathbf{a}_2 + n_3\mathbf{a}_3$, where the $\mathbf{a}_i$ (i=1,2,3) are any non-coplanar vectors and the n_i (i=1,2,3) are integers[5]. The vectors $\mathbf{a}_i$ that span the lattice are referred to as primitive vectors; the set of primitive vectors for a certain Bravais lattice is not unique. A primitive cell for a Bravais lattice is defined as a volume of space that can be translated through every Bravais lattice vector and fill all of space, without overlapping itself or leaving voids. The primitive cell must contain a single lattice point (and possible additional points on its surface). Again, the choice of the primitive cell is not unique and the most common is the Wigner-Seitz cell. The Wigner-Seitz cell around a lattice point is defined as the region that is closer to that point than any other lattice point; it shows the full symmetry of the Bravais lattice. Therefore, a physical crystal can be described by the underlying Bravais lattice and a

basis, which specifies the arrangement of the ions (or, less frequently, atoms or molecules) within a given primitive cell.

An important concept in the description of crystals is the reciprocal lattice. Given a Bravais lattice and a plane wave $e^{i\mathbf{k}\cdot\mathbf{r}}$, for special values of the wavevector $\mathbf{k}$ the plane wave will display the same periodicity as the Bravais lattice. The set of all wavevectors $\mathbf{G}$ that yield plane waves with the periodicity of a Bravais lattice is called the reciprocal lattice. For $\mathbf{R}$ in the Bravais lattice, any wavevector $\mathbf{G}$ in its reciprocal lattice must satisfy the relation $e^{i\mathbf{G}\cdot\mathbf{R}} = 1$. It can be shown that the reciprocal lattice is a Bravais lattice spanned by the primitive vectors

$$\begin{aligned}
\mathbf{b}_1 &= 2\pi \frac{\mathbf{a}_2 \times \mathbf{a}_3}{\mathbf{a}_1 \cdot (\mathbf{a}_2 \times \mathbf{a}_3)}, \\
\mathbf{b}_2 &= 2\pi \frac{\mathbf{a}_3 \times \mathbf{a}_1}{\mathbf{a}_1 \cdot (\mathbf{a}_2 \times \mathbf{a}_3)}, \\
\mathbf{b}_3 &= 2\pi \frac{\mathbf{a}_1 \times \mathbf{a}_2}{\mathbf{a}_1 \cdot (\mathbf{a}_2 \times \mathbf{a}_3)},
\end{aligned} \tag{1.9}$$

where the vectors $\mathbf{a}_i$ (i=1,2,3) are the primitive vectors of the associated Bravais lattice. The relation $\mathbf{b}_i \cdot \mathbf{a}_j = 2\pi\delta_{ij}$ holds. Any vector in the reciprocal lattice can be expressed as $\mathbf{G} = k_1\mathbf{b}_1 + k_2\mathbf{b}_2 + k_3\mathbf{b}_3$, with the k_i (i=1,2,3) being integer coefficients The Wigner-Seitz cell of a reciprocal lattice is called the first Brillouin zone.

Bloch's theorem and band structure

The problem of electrons in a crystalline solid can be cast in the form of a many-electron problem in the Born-Oppenheimer approximation. Since the positive ions in an ideal crystal are arranged in a perfectly periodic configuration, the external potential that acts on the electrons has the periodicity of the Bravais lattice of the crystal

$$U(\mathbf{r}) = U(\mathbf{r} + \mathbf{R}) \tag{1.10}$$

where $\mathbf{R}$ is any Bravais lattice vector[5]. In the free electron approximation, the electrons do not interact with each other and move in an effective potential, with the same periodicity of Eq.(1.10), that accounts for their mutual interaction as well. Independent electrons subject to a potential with the periodicity of a Bravais lattice are called Bloch electrons. Each one of them obeys a one-particle time-independent Schrödinger equation and their stationary eigenstates have a fundamental property given by Bloch's theorem, which can be stated as follows.

Theorem 1.3.1 (Bloch's theorem)**.** *The eigenstates Ψ of the one-electron Hamiltonian $\hat{H} = -\frac{\nabla^2}{2} + U(\mathbf{r})$, where $U(\mathbf{r}) = U(\mathbf{r} + \mathbf{R})$ for any Bravais lattice vector $\mathbf{R}$, can be*

factorized as a plane wave times a function with the periodicity of the Bravais lattice

$$\psi_{n\mathbf{k}}(\mathbf{r}) = e^{i\mathbf{k}\cdot\mathbf{r}} u_{n\mathbf{k}}(\mathbf{r}) \tag{1.11}$$

with $u_{n\mathbf{k}}(\mathbf{r})$ *such that* $u_{n\mathbf{k}}(\mathbf{r}) = u_{n\mathbf{k}}(\mathbf{r}+\mathbf{R})$ *for any Bravais lattice vector.*

This formulation of the Bloch theorem implies that

$$\psi_{n\mathbf{k}}(\mathbf{r}+\mathbf{R}) = e^{i\mathbf{k}\cdot\mathbf{R}} \psi_{n\mathbf{k}}(\mathbf{r}). \tag{1.12}$$

It can be shown that the wavevector $\mathbf{k}$ is real and can take only certain values when boundary conditions of macroscopic periodicity are imposed on these wavefunctions (Born-von Karman conditions). This means setting

$$\psi_{n\mathbf{k}}(\mathbf{r}+N_i\mathbf{a_i}) = \psi_{n\mathbf{k}}(\mathbf{r}) \qquad (i=1,2,3) \tag{1.13}$$

where the $\mathbf{a_i}$ are primitive vectors identifying the unit cell of the crystal and the N_i are integers each of order $N^{\frac{1}{3}}$, N being the total number of primitive cells in the crystal. Consequently, $\mathbf{k}$ is in the form

$$\mathbf{k} = \sum_i \frac{m_i}{N_i}\mathbf{b_i} \tag{1.14}$$

where the m_i are integers and $\mathbf{b_i}$ are the reciprocal lattice vectors such that $\mathbf{b_i}\cdot\mathbf{a_j} = 2\pi\delta_{ij}$. It is noteworthy that, in the limit of a macroscopic crystal ($N\to\infty$), the set of $\mathbf{k}$ vectors in the form of Eq.(1.14) becomes dense in k-space and $\mathbf{k}$ can be considered a continuous variable. The Bloch wavefunctions are thus endowed with the Fourier expansion

$$\psi_{n\mathbf{k}}(\mathbf{r}) = \sum_{\mathbf{G}} c_{n,\mathbf{k}+\mathbf{G}} e^{i(\mathbf{k}+\mathbf{G})\cdot\mathbf{r}} \tag{1.15}$$

where $\mathbf{G}$ is a reciprocal lattice vector.

Several important remarks can be made about Bloch's theorem. The index n that labels the Bloch wavefunctions $\psi_{n\mathbf{k}}$ appears because, for a given $\mathbf{k}$, several solutions to the eigenvalue problem for the Hamiltonian $\hat{H}$ of Th.(1.3.1) exist. Furthermore, the quantum number n is discrete because of the periodic boundary condition imposed on the periodic part of the wavefunction $u_{n\mathbf{k}}(\mathbf{r})$; for each $\mathbf{k}$, there is a set of discretely spaced eigenvalues of $\hat{H}$ $\epsilon_{n\mathbf{k}}$ to which the eigenfunctions $\psi_{n\mathbf{k}}$ belong. The eigenvalues are continuous functions of the variable $\mathbf{k}$. If one lets $\mathbf{k}$ range through all of k-space, a final remark can be made: for a given n, the eigenvalues $\epsilon_{n\mathbf{k}}$ are periodic functions of $\mathbf{k}$ in the reciprocal lattice: $\epsilon_{n\mathbf{k}} = \epsilon_{n\mathbf{k}+\mathbf{G}}$. Therefore, the wavevector $\mathbf{k}$, which is a quantum number called crystal momentum, can be confined to the first Brillouin zone of the crystal. For any n, the set of electronic levels specified by $\epsilon_{n\mathbf{k}} = \epsilon_n(\mathbf{k})$ is called an energy band: it has an upper and lower bound and all the energy levels $\epsilon_{n\mathbf{k}}$ lie in the band of energies between these limits. In semiconductors and insulators, band gaps where there cannot

be any eigenstate for any $\mathbf{k}$ arise; a certain number of bands is completely filled while the others remain empty, and the band gap is the difference between the lowest unoccupied level and the highest occupied level. In metals there are no band gaps between empty and filled states and some bands are partially filled. The Fermi energy ϵ_F, which is the energy of the highest occupied level, intersects one or more bands.

Density of states

It is useful to define the density of states (DOS) for a crystal in the macroscopic limit. The density of states per unit volume $g(\epsilon)$ describes the number of allowed energy states per unit volume and unit energy range. It allows one to calculate quantities q that are weighted sums over one-electron quantities Q dependent on the energy, which become integrals for large crystals

$$q = \int \mathrm{d}\epsilon g(\epsilon) Q(\epsilon). \tag{1.16}$$

The total DOS is clearly given by $g(\epsilon) = \sum_n g_n(\epsilon)$, where $g_n(\epsilon)$ is the density of states of the n-th band[5]. It can be noted that

$$g_n(\epsilon)\mathrm{d}\epsilon = \frac{2}{V_{cell}} \times (\#\,\text{of allowed}\,\mathbf{k}\,\text{in the}\,n\text{-th band in the energy range}\,[\epsilon, \epsilon + \mathrm{d}\epsilon]); \tag{1.17}$$

the factor 2 accounts for spin-degeneracy, V_{cell} is the volume of a primitive cell. The number of allowed wavectors in Eq.(1.17) is the ratio between the k-space volume identified by $\epsilon \leq \epsilon_n(\mathbf{k}) \leq \epsilon + \mathrm{d}\epsilon$ and the volume per allowed wavevector $\mathbf{k}$, equal to $\frac{(2\pi)^3}{V_{cell}}$. This yields an integral in k-space over the volume identified by $\epsilon \leq \epsilon_n(\mathbf{k}) \leq \epsilon + \mathrm{d}\epsilon$, which can in turn be written as the surface integral

$$g_n(\epsilon)\mathrm{d}\epsilon = \int_{S_n(\epsilon)} \frac{dS}{4\pi^3} \delta k(\mathbf{k}). \tag{1.18}$$

$S_n(\epsilon)$ is the portion of the constant-energy surface in k-space given by $\epsilon_n(\mathbf{k}) = \epsilon$ that lies within the primitive cell; the infinitesimal $\delta k(\mathbf{k})$ is the distance between the surfaces $S_n(\epsilon)$ and $S_n(\epsilon + \mathrm{d}\epsilon)$ at point $\mathbf{k}$. Finally, by expressing the infinitesimal variation of the energy in k-space as $\mathrm{d}\epsilon = |\nabla_{\mathbf{k}} \epsilon_n(\mathbf{k})| \delta k(\mathbf{k})$, an expression for the density of states per unit volume of the n-th band is obtained

$$g_n(\epsilon) = \int_{S_n(\epsilon)} \frac{dS}{4\pi^3} \frac{1}{|\nabla_{\mathbf{k}} \epsilon_n(\mathbf{k})|}. \tag{1.19}$$

The singularities of the integrand in Eq.(1.19) due to the vanishing of $|\nabla_{\mathbf{k}} \epsilon_n(\mathbf{k})|$ are integrable in three dimensions; however, they yield discontinuities in the slope of $g_n(\epsilon)$. These singularities are referred to as Van Hove singularities.

1.4 Density functional theory

Density functional theory (DFT) is one of the most popular and successful approaches to the many-body Schrödinger problem. It is widely applied to calculations in chemistry, condensed matter physics and nanoscience. DFT is referred to as an *ab initio* (or first-principles) method: this means that calculations do not include any empirical parameter that has to be adjusted for the specific system[6]. *Ab initio* methods aim to predict chemical and physical properties of a system starting from its chemical composition and fundamental laws. DFT is an exact many-body theory, but in the vast majority of cases its practical applications offer approximate solutions to the many-body problem. Nevertheless, DFT calculations attain a rather high accuracy for a variety of systems and provide a notable reduction in computational costs compared to other techniques[7].

For a system of N interacting electrons, the usual method to calculate the value of observables consists in specifying the external potential $V_{ext}(\mathbf{r})$ that acts on them, solving the time-independent Schrödinger equation for the corresponding electronic Hamiltonian and finally calculating the observables by taking expectation values of the associated operators in the states of the system. One of the observables calculated in this way is the particle density. The particle density in the state Ψ is given by

$$n(\mathbf{r}) = N \int \mathrm{d}\mathbf{x}_2 \int \mathrm{d}\mathbf{x}_3 \cdots \int \mathrm{d}\mathbf{x}_N \Psi^*(\mathbf{r}, \mathbf{x}_2, \ldots, \mathbf{x}_N)\Psi(\mathbf{r}, \mathbf{x}_2, \ldots, \mathbf{x}_N). \tag{1.20}$$

In the context of density-functional theory, the ground-state particle density is considered to be the fundamental variable that allows one to calculate the value of observables instead of the wavefunction that encodes the state of the system. The convenience of this way of proceeding lies in the fact that, in order to study the properties of the system, one needs to determine a function depending on 3 position coordinates rather than the many-electron wavefunction, which depends on 3N position coordinates.

1.4.1 The Hohenberg-Kohn theorems

The modern formulation of density functional theory relies on the Hohenberg-Kohn theorems, first stated in a famous paper in 1964[8]. Hohenberg and Kohn proved that the density of particles in the ground state of a quantum many-body system can be regarded as a "basic variable": all properties of the system are unique functionals of the ground-state density. The original article focuses on a system of interacting electrons in an external potential $V_{ext}(\mathbf{r})$ (such as the one due to nuclei in the Born-Oppenheimer approximation), but their findings apply to all systems composed of interacting particles in an external potential. The first Hohenberg-Kohn theorem can be formulated as follows.

Theorem 1.4.1 (First Hohenberg-Kohn theorem)**.** *For any system of interacting electrons in an external potential $V_{ext}(\mathbf{r})$, the potential $V_{ext}(\mathbf{r})$ is uniquely determined, except for a constant, by the ground-state particle density $n_0(\mathbf{r})$ of the system.*

Corollary 1.4.2. *Since the Hamiltonian of the system is uniquely determined up to a constant, the many-body wavefunctions for all states are determined. Therefore, all properties of the system are fully determined by the ground-state density* $n_0(\mathbf{r})$.

The proof of the first theorem is based on the derivation of a bijection between the external potential V_{ext} and the ground-state density n_0; two external potentials differing by more than a constant yield different ground-state densities. The ground state is assumed to be non-degenerate, but the proof can be readily extended to the case of a degenerate ground-state. The second Hohenberg-Kohn theorem is stated as follows.

Theorem 1.4.3 (Second Hohenberg-Kohn theorem)**.** *It is possible to define a functional for the total energy* $E[n]$ *in terms of the density* $n(\mathbf{r})$*, valid for any external potential* $V_{ext}(\mathbf{r})$*. For a given* $V_{ext}(\mathbf{r})$*, the ground-state energy of the system is the global minimum of the functional* $E[n]$ *and the density that minimizes this functional is the ground-state density* $n_0(\mathbf{r})$.

Corollary 1.4.4. *The functional* $E[n]$ *alone is sufficient to determine the exact ground-state energy and density.*

The original proof of the second theorem is restricted to V-representable densities (i.e. ground-state densities of a system identified by an actual external potential V_{ext}), but it is possible to relax this assumption. The functional for the total energy of the electrons of Th.(1.4.3) can be expressed as

$$E[n] = T[n] + E_{int}[n] + \int \mathrm{d}\mathbf{r} n(\mathbf{r}) V_{ext}(\mathbf{r}) \equiv F_{HK}[n] + \int \mathrm{d}\mathbf{r} n(\mathbf{r}) V_{ext}(\mathbf{r}), \tag{1.21}$$

with the Hohenberg-Kohn functional $F_{HK}[n]$ including all the intrinsic contributions (kinetic and potential) to the total energy. Since it is independent of the specific external potential acting on the electrons, $F_{HK}[n]$ it is also referred to as "universal functional". For a system described by the many-electron Hamiltonian $\hat{H}_e$, the second Hohenberg-Kohn theorem provides a strategy to determine the ground-state energy E_0, the ground-state density n_0 and, as a consequence, the ground-state wavefunction Ψ_0: one needs to look for the minimum of the total energy functional

$$E_0 = E[n_0] = \langle \Psi_0 | \hat{H}_e | \Psi_0 \rangle = \min_{\Psi} \langle \Psi | \hat{H}_e | \Psi \rangle = \min_{\mathrm{n}} E[n]. \tag{1.22}$$

This enables the determination of all other ground-state properties. In general, the excited states $\Psi \neq \Psi_0$ and excited-state properties have to be calculated by a different procedure. Although the method for calculating the ground-state density is given, the Hohenberg-Kohn theorems provide no method to obtain an explicit expression for the energy functional $E[n]$.

1.4.2 The Kohn-Sham equations

Density functional theory is the most widely used method for electronic-structure calculations due to the Kohn-Sham approach, which was built upon the Hohenberg-Kohn formalism. In an article published in 1965, Kohn and Sham proposed replacing the many-body system of interacting electrons with a simpler auxiliary system[9]. The construction of the auxiliary system is based on a fundamental ansatz: the exact ground-state density for the many-electron system can be represented as the ground-state density of an auxiliary system of non-interacting particles. The Hamiltonian of the auxiliary system features two terms: the standard kinetic operator and a certain local effective potential $V_{eff}(\mathbf{r})$ acting on an electron at point $\mathbf{r}$. This leads to a system of independent-particle equations that can be considered exactly soluble. Their solution yields the ground-state density and energy of the many-electron system; in principle, every property of the original system is thus determined. The auxiliary Hamiltonian is

$$\hat{H}_{aux} = -\frac{1}{2}\nabla^2 + V_{eff}(\mathbf{r}). \tag{1.23}$$

For a system of N independent electrons obeying the Hamiltonian in Eq.(1.23), the ground state has one electron in each of the N orbitals $\psi_i(\mathbf{r})$ belonging to the lowest eigenvalue ϵ_i of the auxiliary Hamiltonian. The ground-state density of the auxiliary system is thus given by the sum of the squared modulus of these orbitals

$$n(\mathbf{r}) = \sum_{i=1}^{N} |\psi_i(\mathbf{r})|^2. \tag{1.24}$$

The total kinetic energy of the auxiliary system T_s can be expressed as

$$T_s = -\frac{1}{2}\sum_{i=1}^{N}\langle\psi_i|\nabla^2|\psi_i\rangle = \frac{1}{2}\sum_{i=1}^{N}\int \mathrm{d}\mathbf{r}|\nabla\psi_i(\mathbf{r})|^2 \tag{1.25}$$

and the classical Coulomb energy that stems from the self-interaction of the electron density $n(\mathbf{r})$ is

$$E_H[n] = \frac{1}{2}\int\int \mathrm{d}\mathbf{r}\mathrm{d}\mathbf{r}'\frac{n(\mathbf{r})n(\mathbf{r}')}{|\mathbf{r}-\mathbf{r}'|}, \tag{1.26}$$

known as the Hartree energy. The Kohn-Sham approach consists in rewriting the energy functional of the ground-state density for the interacting many-electron system as

$$E_{KS}[n] = T_s[n] + E_H[n] + \int \mathrm{d}\mathbf{r}V_{ext}(\mathbf{r})n(\mathbf{r}) + E_{xc}[n] \tag{1.27}$$

where $V_{ext}(\mathbf{r})$ is the external potential due to the nuclei and any other external fields (assumed to be independent of spin). The term $E_{xc}[n]$ in Eq.(1.27) is the exchange-correlation energy functional. Comparing Eq.(1.21) and Eq.(1.27), the following expression for the exchange-correlation functional is found:

$$E_{xc}[n] = F_{HK}[n] - T_s[n] - E_H[n] = T[n] - T_s[n] + E_{int}[n] - E_H[n]. \tag{1.28}$$

$E_{xc}[n]$ represents the difference between the kinetic and the internal interaction energies of the true interacting many-electron system and those of the Kohn-Sham auxiliary system; it clearly accounts for all the many-body effects of exchange and correlation. The ground-state density for the interacting system is determined, while imposing orthonormalization constraints on the ψ_i orbitals, by minimizing E_{KS} with respect to ψ_i^*. This is equivalent to solving the Kohn-Sham equations

$$\hat{H}_{aux}\psi_i(\mathbf{r}) = \left[-\frac{1}{2}\nabla^2 + V_{KS}(\mathbf{r})\right]\psi_i(\mathbf{r}) = \epsilon_i\psi_i(\mathbf{r}) \tag{1.29}$$

with the local effective potential

$$V_{KS}(\mathbf{r}) = V_{ext}(\mathbf{r}) + \frac{\delta E_H}{\delta n(\mathbf{r})} + \frac{\delta E_{xc}}{\delta n(\mathbf{r})} = V_{ext}(\mathbf{r}) + V_H(\mathbf{r}) + V_{xc}(\mathbf{r}), \tag{1.30}$$

which constitute a set of Schrödinger-like independent-particle equations. The ground-state density of the many-electron system is then given by Eq.(1.24).

The solution of the Kohn-Sham equations would ideally lead to the exact ground-state energy and density of the interacting many-electron system; all other ground-state properties could consequently be determined. However, the equations are coupled and must be solved through a self-consistent cycle. An initial guess for the electronic ground-state density $n(\mathbf{r})$ determines the effective potential $V_{eff}(\mathbf{r})$, which in turn is used to solve the Kohn-Sham equations. If n does not coincide with the exact ground-state density, it will differ from the electron density given by the solutions of the single-particle equations where V_{eff} has been inserted. The new electron density yielded by the solutions of the Kohn-Sham equations is used to calculate a new effective potential. This procedure is reiterated until the difference between the ground-state densities obtained at two consecutive iterations is smaller than a chosen convergence threshold. If the exchange-correlation energy functional $E_{xc}[n]$ were known, the only approximation coming into play in a calculation of the ground-state density would be the one arising from the numerical method employed to solve the Kohn-Sham equations. Because of the intricacies of the many-electron problem, the explicit expression for the exchange-correlation functional is too complex to be computed. Nonetheless, a variety of approximations have been found over time and are successfully employed in DFT calculations.

1.4.3 Implementation

Density functional theory is the primary tool for predicting structural and electronic properties of solid systems in condensed matter physics. The present section looks at the main strategies and approximations used in actual DFT calculations.

Approximations for the exchange-correlation functional

The accuracy and computational cost of a DFT calculation depend on the chosen approximation for the exchange-correlation functional $E_{xc}[n]$. It can be written in the general form

$$E_{xc}[n] = \int \mathrm{d}\mathbf{r} n(\mathbf{r}) \epsilon_{xc}([n], \mathbf{r}) \tag{1.31}$$

for slowly-varying densities; $\epsilon_{xc}([n], \mathbf{r})$ is the energy per electron at point $\mathbf{r}$, which depends on the density $n(\mathbf{r})$ in some neighborhood of point $\mathbf{r}$[4]. The most important approximation, which was already suggested by Kohn and Sham in their 1965 paper, is the local density approximation (LDA or LSDA for spin polarized calculations): it still serves as a basis for the construction of modern exchange-correlation functionals. The core idea of the LDA is to locally treat the system of interest as an homogeneous electron gas with the same density of the real system at that point. The effects of exchange and correlation are local for an homogeneous electron gas. The exchange–correlation energy density at each point is considered to be the same as in a homogeneous electron gas with that density; the exchange–correlation energy functional in the LDA thus becomes

$$\begin{aligned} E_{xc}^{LDA}[n] &= \int \mathrm{d}\mathbf{r} n(\mathbf{r}) \epsilon_{xc}^{hom}(n(\mathbf{r})) \\ &= \int \mathrm{d}\mathbf{r}\, n(\mathbf{r}) [\epsilon_x^{hom}(n(\mathbf{r})) + \epsilon_c^{hom}(n(\mathbf{r}))]. \end{aligned} \tag{1.32}$$

The exchange term ϵ_x^{hom} in the exchange–correlation energy density has a simple analytical expression, while the correlation term ϵ_c^{hom} has been calculated through MonteCarlo methods.

The LDA paved the way for the construction of generalized-gradient approximations (GGAs) for the exchange-correlation functional. Compared with LDA, these approximations lead to more accurate predictions of total energies, atomization energies and energy barriers[10] and are the standard used in solid-state physics calculations[4]. The general form for an exchange-correlation energy functional in the GGA approximation is

$$\begin{aligned} E_{xc}^{GGA}[n] &= \int \mathrm{d}\mathbf{r} n(\mathbf{r}) \epsilon_{xc}(n, |\nabla n|) \\ &= \int \mathrm{d}\mathbf{r}\, n(\mathbf{r}) \epsilon_x^{hom}(n) F_{xc}(n, |\nabla n|) \end{aligned} \tag{1.33}$$

where F_{xc} is a dimensionless function of the density and the density gradient for each spin and ϵ_x^{hom} is the exchange energy of the unpolarized homegeneous electron gas of density $n(\mathbf{r})$. One of the most popular GGA functionals is the Perdew-Burke-Enzerhof functional (PBE)[10]; it is used to benchmark codes in the condensed-matter community. A huge variety of functionals that go beyond the local density and generalized-gradient

approximations has been developed through different methods of increasing capability and complexity, such as meta-GGA functionals, hybrid functionals and RPA functionals.

Plane wave basis

The Kohn-Sham auxiliary system for electrons in a crystalline solid is composed of non-interacting electrons moving in the effective Kohn-Sham potential, which has the same periodicity of the Bravais lattice of the crystal. Therefore, the electrons in the auxiliary system are Bloch electrons and the Kohn-Sham equations will have solutions in the form of Eq.(1.15). Expanding the Kohn-Sham orbitals in a plane wave basis has several advantages in calculations; however, it is not possible to compute the terms of the expansion for each of the infinite $\mathbf{G}$ vectors. A parameter called "cut-off energy" is then introduced in the calculation: it sets a limit to the kinetic energy of the plane waves included in the expansion of the Kohn-Sham orbitals[11]. If the cut-off energy is E_{cut}, only the terms corresponding to $\mathbf{G}$ vectors that satisfy the condition

$$\frac{1}{2}|\mathbf{k}+\mathbf{G}|^2 \leq E_{cut} \tag{1.34}$$

are computed; the contribution of plane waves that have a higher kinetic energy is disregarded, as it is less physically relevant. The choice of the cut-off energy affects both the accuracy and the computational cost of a calculation, so convergence with respect to E_{cut} has to be achieved.

As previously mentioned, in the limit of a macroscopic crystal, the spacing between the allowed $\mathbf{k}$ vectors in the reciprocal space vanishes, $\mathbf{k}$ becomes a continuous variable and all summations over the reciprocal space are reduced to integrals. In DFT calculation for a large crystal, integrals over the first Brillouin zone in the form

$$\overline{f} = \frac{V_{cell}}{(2\pi)^3}\int_{B.Z.} \mathrm{d}\mathbf{k} f(\mathbf{k}) \tag{1.35}$$

have to be evaluated; V_{cell} is the volume of a primitive cell of the crystal and $\frac{(2\pi)^3}{V_{cell}}$ is the volume of the first Brillouin zone[11]. In practice, these integrals have to be computed by numerical methods: they are reduced to weighted summations of the values of f at a discrete set of k-points in the Brillouin zone. One of the most widespread and efficient techniques to calculate integrals in the form of Eq.(1.35) is the Monkhorst-Pack method. To use it, a grid of k-points is built to sample the Brillouin zone, specifying the number of k-points included for each direction; if the calculation is performed on a cell defined by lattice vectors with equal length, it is natural to choose the same number of k-points for each direction. Given that an increasing density of the k-point grid is associated with increasing accuracy and computational toll, convergence with respect to the k-point grid has to be achieved. However, the convergence for metals

might be slow and difficult to reach. This is due to the fact that, for metals in the ground state, the Brillouin zone is divided by the Fermi surface in regions that are occupied and unoccupied by electrons; the integrands thus show abrupt discontinuities at the Fermi surface. The two main strategies to tackle this obstacle are the tetrahedron method[12] and the smearing methods. The latter entail modifying the integrand in order to remove the discontinuity with the introduction of an additional term dependent on a smearing parameter; the former consists in subdividing the Brillouin zone in non-overlapping tetrahedra and defining the integrand at every point in a tetrahedron using linear interpolation.

Pseudopotentials

While studying the electronic states in a solid, it is useful to separate the valence states from the core states: the latter do not change significantly between free atoms and solids and do not influence the chemical properties of the material, whereas the former are responsible for the bonding and low-energy properties of the material[2]. The pseudopotential method enables the description of valence states without treating the core states. The essential strategy is to replace the strong Coulomb potential of the nuclei, tightly binding the core electrons, with a weak pseudopotential, which should lead to an efficient determination of the conduction and valence bands; the pseudopotential coincides with the original potential outside the core regions. As a consequence, the corresponding pseudowavefunctions should represent the original crystalline wavefunctions outside the core regions; on the other hand, within the core regions smoothing can occur.

It is important to note that for a free atom, outside the core region, the radial wavefunction and the corresponding pseudowavefunction are proportional to each other, but in general are not exactly equal. The solution of the radial Schrödinger equation (at the same energy) for each potential yields the same wavefunction up to a normalization factor in the region where the pseudopotential and true potential coincide; the normalization constants usually differ, as they also depend on the behaviour of the wavefunctions in the core region.

The first pseudopotentials that appeared in solid-state physics were empirical. A milestone for the theory of pseudopotentials was the advent of *ab initio* norm-conserving pseudopotentials in a 1979 article by Hamann, Schlüter, and Chiang[13]. The main idea behind norm-conserving pseudopotentials is to impose the exact agreement of the true atomic wavefunctions and the corresponding pseudowavefunctions beyond a chosen "core radius" r_c. This entails the property of norm conservation; in other words, the integrals from the origin to a radius r of the real and pseudo charge densities agree if $r > r_c$ for each valence state. Norm conservation ensures optimal transferability of the pseudopotential among several chemical environments in self-consistent calculations relying on the charge density. If the pseudowavefunctions of the isolated atom coincide with those of the true atom outside the core region, the pseudoatom will behave like the true one, even in a

different setting (e.g. in a solid). Kleinman proved that the Hamann-Schlüter-Chiang pseudopotential can be generalized to include relativistic corrections, allowing one to treat heavy atoms in a convenient non-relativistic formalism[14].

1.5 Optical properties

1.5.1 Time-dependent density functional theory

The success of density functional theory in the treatment of the stationary many-body problem ignited the interest of the scientific community in approaching time-dependent many-body problems -such as scattering processes and photoabsorption- through the DFT formalism. The dynamics of a many-body system that evolves over time is described by the time-dependent Schrödinger equation

$$i\frac{\partial\Psi(t)}{\partial t} = \hat{H}(t)\Psi(t) \tag{1.36}$$

with the initial condition $\Psi(t=0) = \Psi_0$; the hamiltonian $\hat{H}(t)$ is assumed to be the sum of three operators representing the kinetic energy, the potential due to the interaction between particles and a local time-dependent external potential:

$$\hat{H}(t) = \hat{T} + \hat{V}_{int} + \hat{V}_{ext}(t). \tag{1.37}$$

The quantum-mechanical action between the instants t_0 and t_1 is defined as

$$A = \int_{t_0}^{t_1} \mathrm{d}t \, \big\langle \Psi(t) \big| i\frac{\partial}{\partial t} - \hat{H}(t) \big| \Psi(t) \big\rangle. \tag{1.38}$$

Time-dependent density functional theory (TDDFT) relies on the formalism presented in an article by Runge and Gross in 1984[15], analogous to the Hohenberg-Kohn formalism, for time-dependent systems obeying the Hamiltonian in Eq.(1.37) . Runge and Gross proved that time-dependent single-particle external potentials $V_{ext}(\mathbf{r}, t)$ acting on the components of the many-body systems are in a one-to-one correspondence with V-representable time-dependent densities $n(\mathbf{r}, t)$. Furthermore, they proved that the quantum-mechanical action can be expressed as a unique functional of the density $A[n]$, which features a stationary point at the exact density of the system. The last finding suggests that, in principle, the exact density of the system at any time can be computed through the minimization of the action with respect to the density, i.e. by imposing

$$\frac{\delta A[n]}{\delta n(\mathbf{r}, t)} = 0. \tag{1.39}$$

Finally, Runge and Gross designed a practical scheme to calculate the density of the system equivalent to the Kohn-Sham formalism, introducing an auxiliary system of non-interacting particles. The exact time-dependent density of the interacting system is yielded by

$$n(\mathbf{r},t) = \sum_i |\psi_i(\mathbf{r},t)|^2 \tag{1.40}$$

where the ψ_i single-particle orbitals are solutions of the time-dependent Schrödinger-like equations

$$\left[-\frac{1}{2}\nabla^2 + V_{KS}(\mathbf{r},t)\right]\psi_i(\mathbf{r},t) = i\frac{\partial\psi_i(\mathbf{r},t)}{\partial t}. \tag{1.41}$$

The effective potential acting on the auxiliary particles in Eq.(1.41) is

$$V_{KS}(\mathbf{r},t) = V_{ext}(\mathbf{r},t) + V_H(\mathbf{r},t) + V_{xc}(\mathbf{r},t); \tag{1.42}$$

as in the stationary case, it is the sum of the external time-dependent potential, the time-dependent potential associated with the Hartree interaction energy and, finally, the exchange-correlation potential. The physical meaning of the exchange-correlation potential is analogous to that of the stationary case and it can be written as

$$V_{xc}(\mathbf{r},t) = \frac{\delta A_{xc}[n]}{\delta n(\mathbf{r},t)}, \tag{1.43}$$

where $A_{xc}[n]$ is the exchange-correlation part of the action functional.

1.5.2 Dielectric function in the TDDFT formalism

The excitation energies and the optical properties of a crystal can be calculated from first principles exploiting time-dependent density functional theory in the linear-response formalism. TDDFT is successfully applied in the description of excitation processes because it manages to take into account their dynamical nature[16].

Linear response theory in TDDFT for periodic systems

A many-body system is considered to be subject to an external potential in the form

$$V_{ext}(\mathbf{r},t) = V_{ext}^{(0)}(\mathbf{r}) + V_{ext}^{(1)}(\mathbf{r},t)\Theta(t-t_0) \tag{1.44}$$

where $V_{ext}^{(1)}(\mathbf{r},t)$ is a small time-dependent perturbation that starts acting on the system at the instant t_0; for $t < t_0$, the system is in the ground state, which is determined by stationary DFT. Time-dependent density functional theory states that the time dependent density $n(\mathbf{r},t)$ is a unique functional of $V_{ext}(\mathbf{r},t)$, thus $n(\mathbf{r},t) = n[V_{ext}](\mathbf{r},t)$; the difference

between the density $n(\mathbf{r},t)$ and the initial ground-state density $n_0(\mathbf{r}) = n_0[V_{ext}^{(0)}](\mathbf{r})$ can be expanded in powers of the perturbation $V_{ext}^{(1)}$

$$n(\mathbf{r},t) - n_0(\mathbf{r}) = n_1(\mathbf{r},t) + O({V_{ext}^{(1)}}^2), \tag{1.45}$$

where $n_1(\mathbf{r},t)$ is the first-order density response of the system

$$n_1(\mathbf{r},t) = \int\int \mathrm{d}t'\mathrm{d}\mathbf{r}'\chi(\mathbf{r},\mathbf{r}',t,t')V_{ext}^{(1)}(\mathbf{r}',t'). \tag{1.46}$$

χ is the density–density response function -also referred to as susceptibility- of the many-body system and, given the functional Taylor expansion in Eq.(1.45), can be expressed as

$$\chi(\mathbf{r},\mathbf{r}',t,t') = \left.\frac{\delta n[V_{ext}](\mathbf{r},t)}{\delta V_{ext}(\mathbf{r}',t')}\right|_{V_{ext}^0[n_0]} \tag{1.47}$$

As previously mentioned, the time-dependent density $n(\mathbf{r},t)$ can be reproduced by a Kohn-Sham time-dependent system of non-interacting particles, subject to the Kohn-Sham effective potential V_{KS} reported in Eq.(1.42); V_{KS} explicitly reads

$$V_{KS}(\mathbf{r},t) = V_{ext}^{(0)}(\mathbf{r}) + V_{ext}^{(1)}(\mathbf{r},t)\Theta(t-t_0) + \int \mathrm{d}\mathbf{r}'\frac{n(\mathbf{r}',t)}{|\mathbf{r}-\mathbf{r}'|} + V_{xc}(\mathbf{r},t). \tag{1.48}$$

The time-dependent density $n(\mathbf{r},t)$ can be written as a unique functional of the Kohn-Sham effective potential $n(\mathbf{r},t) = n[V_{KS}](\mathbf{r},t)$. Following analogous steps to the many-body system case, the first-order density response is

$$n_1(\mathbf{r},t) = \int\int \mathrm{d}t'\mathrm{d}\mathbf{r}'\chi_0(\mathbf{r},\mathbf{r}',t,t')V_{KS}^{(1)}(\mathbf{r}',t'). \tag{1.49}$$

In Eq.(1.49), χ_0 is the independent-particle density-density response function

$$\chi_0(\mathbf{r},\mathbf{r}',t,t') = \left.\frac{\delta n[V_{KS}](\mathbf{r},t)}{\delta V_{KS}(\mathbf{r}',t')}\right|_{V_{KS}[n_0]} \tag{1.50}$$

and the linearized effective potential $V_{KS}^{(1)}$ is the sum of the external perturbation, the linearized Hartree potential and the linearized exchange-correlation potential

$$\begin{aligned} V_{KS}^{(1)}(\mathbf{r},t) = V_{KS}[n]^{(1)}(\mathbf{r},t) = V_{ext}^{(1)}(\mathbf{r},t) &+ \int \mathrm{d}\mathbf{r}'\frac{n_1(\mathbf{r}',t)}{|\mathbf{r}-\mathbf{r}'|} \\ &+ \int\int \mathrm{d}t'\mathrm{d}\mathbf{r}' f_{xc}(\mathbf{r},\mathbf{r}',t,t')n_1(\mathbf{r}',t). \end{aligned} \tag{1.51}$$

The exchange-correlation term in Eq.(1.51) features the exchange-correlation kernel

$$f_{xc}(\mathbf{r},\mathbf{r}',t,t') = \left.\frac{\delta V_{xc}[n](\mathbf{r},t)}{\delta n(\mathbf{r}',t')}\right|_{n_0}. \tag{1.52}$$

The kernel f_{xc} is a functional of the ground-state density $n_0(\mathbf{r})$ and is a key quantity of TDDFT in the linear-response regime, as it embodies the dynamical many-body effects that come into play in a transition to an excited state. By equating Eqs.(1.46) and (1.49), a relation linking the susceptibilities for the many-body system, χ, and for the Kohn-Sham system, χ_0, is found; if transformed into the frequency domain, it yields the Dyson-like equation

$$\begin{aligned}\chi(\mathbf{r},\mathbf{r}',\omega) &= \chi_0(\mathbf{r},\mathbf{r}',\omega) \\ &+ \int\int \mathrm{d}\mathbf{x}\mathrm{d}\mathbf{x}'\, \chi_0(\mathbf{r},\mathbf{x},\omega)\left\{\frac{1}{|\mathbf{x}-\mathbf{x}'|} + f_{xc}(\mathbf{x},\mathbf{x}',\omega)\right\}\chi(\mathbf{x}',\mathbf{r}',\omega).\end{aligned} \tag{1.53}$$

In a periodic solid, the susceptibility $\chi(\mathbf{r},\mathbf{r}',\omega)$ must show the same translational symmetry properties of the Bravais lattice; as a consequence, it is endowed with the Fourier expansion

$$\chi(\mathbf{r},\mathbf{r}',\omega) = \frac{1}{V}\sum_{\mathbf{k}\in \mathrm{BZ}}\sum_{\mathbf{G},\mathbf{G}'} e^{-i(\mathbf{k}+\mathbf{G})\cdot\mathbf{r}} e^{i(\mathbf{k}+\mathbf{G}')\cdot\mathbf{r}'}\chi(\mathbf{k}+\mathbf{G},\mathbf{k}+\mathbf{G}',\omega); \tag{1.54}$$

$\mathbf{k}$ is a vector in the first Brillouin zone, $\mathbf{G}$ and $\mathbf{G}'$ are reciprocal lattice vectors and V is the volume of the crystal. $\chi(\mathbf{k}+\mathbf{G},\mathbf{k}+\mathbf{G}',\omega)$ will be denoted as $\chi_{\mathbf{G}\mathbf{G}'}(\mathbf{k},\omega)$ throughout. Therefore, Eq.(1.53) in the reciprocal space can be cast as

$$\begin{aligned}\chi_{\mathbf{G}\mathbf{G}'}(\mathbf{k},\omega) &= \chi_{0\mathbf{G}\mathbf{G}'}(\mathbf{k},\omega) \\ &+ \sum_{\mathbf{G}_1,\mathbf{G}_2}\chi_{0\mathbf{G}\mathbf{G}_1}(\mathbf{k},\omega)\left\{v_{\mathbf{G}_1}(\mathbf{k})\delta_{\mathbf{G}_1\mathbf{G}_2} + f_{xc\mathbf{G}_1\mathbf{G}_2}(\mathbf{k},\omega)\right\}\chi_{\mathbf{G}_2\mathbf{G}'}(\mathbf{k},\omega),\end{aligned} \tag{1.55}$$

where $v_{\mathbf{G}}(\mathbf{k})$ is the Fourier transform of the Coulomb potential $v_{\mathbf{G}}(\mathbf{k}) = \frac{4\pi}{|\mathbf{k}+\mathbf{G}|^2}$. The inverse dielectric function ϵ^{-1}, that represents the screening in the system, can be defined as

$$\epsilon^{-1}(\mathbf{r},\mathbf{r}',t,t') = \frac{\delta V_{KS}(\mathbf{r},t)}{\delta V_{ext}(\mathbf{r}',t')}; \tag{1.56}$$

in a periodic solid, its expression in the reciprocal space is related to the susceptibility χ by the equation

$$\epsilon^{-1}_{\mathbf{G}\mathbf{G}'}(\mathbf{k},\omega) = \delta_{\mathbf{G}\mathbf{G}'} + v_{\mathbf{G}}(\mathbf{k})\chi_{\mathbf{G}\mathbf{G}'}(\mathbf{k},\omega) \tag{1.57}$$

It is important to highlight that the expressions of the susceptibility χ and the inverse dielectric function ϵ^{-1}, both in real and momentum space, depend on the exchange-correlation kernel f_{xc} (or its Fourier transform). Clearly, as the exact many-body

exchange-correlation contributions are unknown, approximate expressions for f_{xc} are employed; the calculated susceptibility and the inverse dielectric function depend on the chosen approximation. The coarsest approximation, called random phase approximation, consists in neglecting the kernel entirely: $f_{xc}^{RPA} = 0$. In the RPA, only the independent-particle susceptibility χ_0 is thus needed to calculate the susceptibility χ and, as a result, the inverse dielectric function ϵ^{-1}. The independent-particle susceptibility in the reciprocal lattice can be written as

$$\begin{aligned}\chi_{0\mathbf{G}\mathbf{G}'}(\mathbf{k},\omega) = \frac{1}{V}\sum_{\mathbf{k}'\in \mathrm{BZ}}\sum_{j,l}\frac{f_{l\mathbf{k}+\mathbf{k}'} - f_{j\mathbf{k}'}}{\omega + \epsilon_{j\mathbf{k}'} - \epsilon_{l\mathbf{k}+\mathbf{k}'} + i\eta} \\ \times \langle j\mathbf{k}'|e^{-i(\mathbf{k}+\mathbf{G})\cdot\mathbf{r}}|l\mathbf{k}+\mathbf{k}'\rangle\langle l\mathbf{k}+\mathbf{k}'|e^{i(\mathbf{k}+\mathbf{G}')\cdot\mathbf{r}'}|j\mathbf{k}'\rangle,\end{aligned} \tag{1.58}$$

where the integer indices are the band indices for the Kohn-Sham auxiliary state of the solid and $\mathbf{k}'$ is a wavevector in the first Brillouin zone of the crystal; the $f_{j\mathbf{k}'}$ are occupation numbers, while the $\epsilon_{j\mathbf{k}'}$ and the $|j\mathbf{k}'\rangle$ are respectively the Kohn-Sham eigenvalues and eigenstates.

The macroscopic dielectric function of a periodic solid

The connection between the quantities defined in the context of linear-response theory and the spectroscopic observables of a macroscopic solid shall now be presented. An electric field $\mathbf{E}$, oscillating with frequency ω in the long-wavelength limit, acts as a small perturbation on a periodic crystal. $\mathbf{E}$ is characterized by a small wavevector $\mathbf{q}$; however, the local electric field inside the crystal will also include terms dependent on wavevectors in the form $\mathbf{q}+\mathbf{G}$, where $\mathbf{G}$ is some reciprocal lattice vector[17]. These components oscillate rapidly over the unit cell and stem from the inhomogeneity at the microscopic scale that every crystal displays, even those characterized by a cubic lattice , yielding isotropic optical properties. At the microscopic scale, the linear polarization effects of the electric field $\mathbf{E}$ on a medium are described by the electric displacement vector $\mathbf{D}$

$$\mathbf{D}(\mathbf{q}+\mathbf{G},\omega) = \sum_{\mathbf{G}'}\epsilon_{\mathbf{G}\mathbf{G}'}(\mathbf{q},\omega)\mathbf{E}(\mathbf{q}+\mathbf{G}',\omega). \tag{1.59}$$

A comparable relation exists between the corresponding macroscopic quantities

$$\mathbf{D}_{mac}(\omega) = \epsilon_{mac}(\omega)\mathbf{E}_{mac}(\omega). \tag{1.60}$$

It can be shown that the macroscopic dielectric function $\epsilon_{mac}(\omega)$ is given by

$$\epsilon_{mac}(\omega) = \lim_{\mathbf{q}\to 0}\left.\frac{1}{\epsilon^{-1}_{\mathbf{G}\mathbf{G}'}(\mathbf{q},\omega)}\right|_{\mathbf{G}=\mathbf{G}'=0}, \tag{1.61}$$

where $\epsilon^{-1}_{\mathbf{G}\mathbf{G}'}(\mathbf{q},\omega)$ is the microscopic inverse dielectric matrix given by Eq.(1.57); the local field effects (LFE) are encoded in the off-diagonal terms of $\epsilon^{-1}_{\mathbf{G}\mathbf{G}'}(\mathbf{q},\omega)$. A calculation of

$\epsilon_{mac}(\omega)$ that includes LFE in the random phase approximation thus entails calculating $\chi_{\mathbf{GG'}}(\mathbf{q},\omega)$ disregarding the Fourier transform of f_{xc} in Eq.(1.55), using $\chi_{\mathbf{GG'}}(\mathbf{q},\omega)$ to calculate $\epsilon^{-1}_{\mathbf{GG'}}(\mathbf{q},\omega)$ and then taking its (0,0) component in the long-wavelength limit $\mathbf{q} \to 0$. A calculation of $\epsilon_{mac}(\omega)$ at the independent-particle level, i.e. neglecting local field effects, can be carried out in a similar way by also disregarding the Coulomb term in Eq.(1.55) and thus imposing $\chi_{\mathbf{GG'}}(\mathbf{q},\omega) = \chi_{0\mathbf{GG'}}(\mathbf{q},\omega)$. The macroscopic dielectric function carries information about the optical absorption and the electron energy loss, which are experimental spectroscopic observables[16]; specifically, the optical absorption spectra of periodic solids are determined *ab-initio* by

$$\mathrm{Abs}(\omega) = \mathrm{Im}(\epsilon_{mac}(\omega)). \tag{1.62}$$

Chapter 2

Results

In this chapter, the results of first-principles calculations of the electronic structure and optical properties of bulk gold and the Au(111) surface are presented. The study is carried out within the framework of density functional theory, employing the Quantum ESPRESSO and YAMBO codes.First, bulk gold is considered. The optimal values of the key computational parameters are determined. The band structure, density of states and projected density of states are then computed, both in the scalar-relativistic regime and including spin-orbit coupling. The optical absorption spectrum is subsequently calculated within the random phase approximation, at the independent-particle level and with the inclusion of local-field effects. The Au(111) surface is then investigated through slab calculations. Slabs of varying thickness are constructed and their surface energy is evaluated. The density of states and layer-resolved projected density of states of several slabs are calculated. Finally, the optical absorption spectra are computed within the random phase approximation, both at the independent-particle level and including local-field effects.

2.1 Bulk Au

This section investigates the ground-state electronic structure and the optical properties of bulk gold through first-principle calculations. All electronic-structure simulations in this section are carried out using the Quantum ESPRESSO integrated suite[18][19], which is based on density functional theory, plane waves and the pseudopotential approach. After the determination of the essential computational parameters, the band structure, density of states and projected density of states of bulk gold are computed, both neglecting and including the spin-orbit effect. Furthermore, calculations of the optical absorption spectrum of scalar-relativistic bulk gold within the random phase approximation are carried out, both at the IP level and including local field effects. The plane-waves, *ab initio* code YAMBO[20][21] is used. The pseudopotentials employed in

all calculations were generated using the ONCVPSP (Optimized Norm-Conserving Vanderbilt PSeudopotential) code[22], either in its scalar-relativistic or in its fully-relativistic version; they include 19 valence electrons. The PBE exchange-correlation functional[10] is employed.

2.1.1 Convergence tests and optimal computational parameters

The calculations for bulk gold are performed on an FCC primitive cell, identified by the primitive vectors

$$\mathbf{a}_1 = \frac{a}{2}(-1,0,1) \quad \mathbf{a}_2 = \frac{a}{2}(0,1,1) \quad \mathbf{a}_3 = \frac{a}{2}(-1,1,0) \tag{2.1}$$

with a single atom positioned at the origin (0,0,0). The parameter a in Eq.(2.1) is the equilibrium lattice parameter. The optimal value of a, which is generally different in the scalar-relativistic and fully-relativistic case, has to be determined, in addition to the cut-off energy E_{cut}, the convergence threshold for the energy E_{thr} and the k-point grid. In order to specify all of these computational parameters, a series of self-consistent calculations of the ground-state total energy is executed. Since gold is a metal, the Gaussian smearing method is employed to facilitate convergence in all calculations reported in this paragraph.

Firstly, the scalar-relativistic case is treated. The smearing parameter, which is the Gaussian broadening σ, is initially set to 0.005 Ry and a fixed $14 \times 14 \times 14$ k-point grid is used to sample the first Brillouin zone. For different convergence thresholds and cut-off energies, the total energies at several values of a are collected and subsequently fitted to the Murnaghan equation of state. The optimal equilibrium lattice parameter a_0 for each convergence threshold and cut-off energy is taken to be the global minimum point of the corresponding fitting curve. The total energies evaluated at each a for varying E_{cut} and their fits are reported in Fig.(2.1), Fig.(2.2) and Fig.(2.3), which respectively correspond to the energy convergence thresholds $E_{thr} = 10^{-6}$ Ry, $E_{thr} = 10^{-9}$ Ry and $E_{thr} = 10^{-12}$ Ry; in the same figures, the variation of a_0 with respect to E_{cut} is presented.

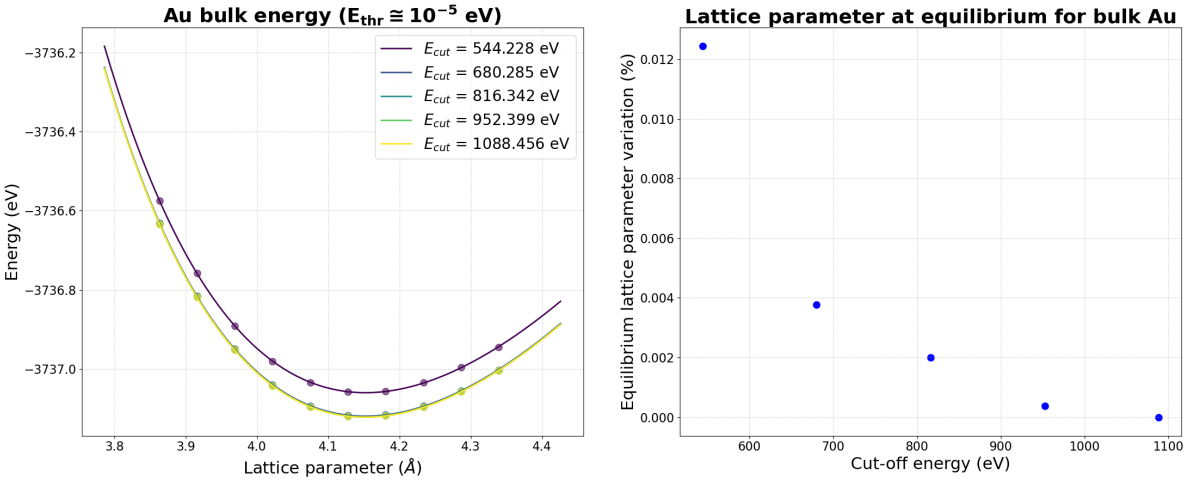

Figure 2.1: Convergence test for the cut-off energy E_{cut} and relative difference between the equilibrium lattice parameter as a function of E_{cut} and its value at maximum cut-off energy, at fixed convergence threshold $E_{thr} = 10^{-6}$ Ry $\cong 10^{-5}$ eV. In the left plot, scatter points represent the data from DFT self-consistent calculations at different E_{cut} values, while continuous lines indicate the respective fits.

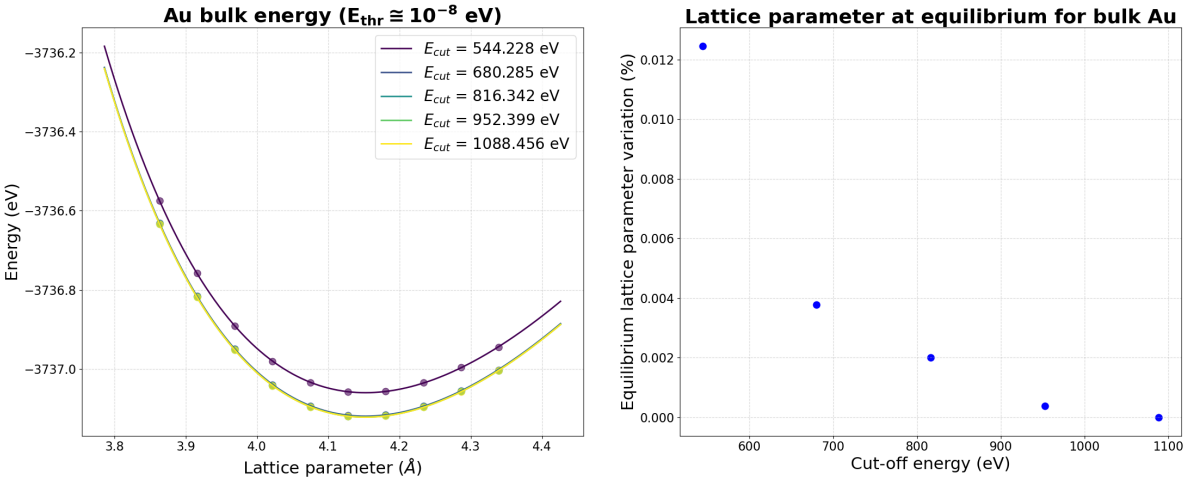

Figure 2.2: Convergence test for the cut-off energy E_{cut} and relative difference between the equilibrium lattice parameter as a function of E_{cut} and its value at maximum cut-off energy, at fixed convergence threshold $E_{thr} = 10^{-9}$ Ry $\cong 10^{-8}$ eV. In the left plot, scatter points represent the data from DFT self-consistent calculations at different E_{cut} values, while continuous lines indicate the respective fits.

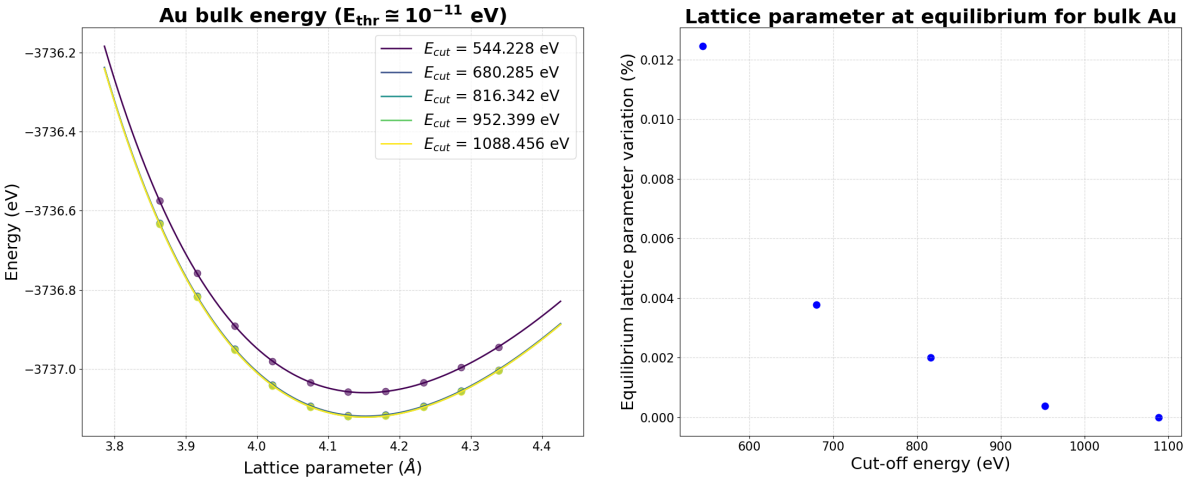

Figure 2.3: Convergence test for the cut-off energy E_{cut} and relative difference between the equilibrium lattice parameter as a function of E_{cut} and its value at maximum cut-off energy, at fixed convergence threshold $E_{thr} = 10^{-12}$ Ry $\cong 10^{-11}$ eV. In the left plot, scatter points represent the data from DFT self-consistent calculations at different E_{cut} values, while continuous lines indicate the respective fits.

As shown in Figs.(2.1)-(2.3), the fitting curves drop to lower energies for increasing E_{cut} and are nearly coincident for cut-off energies equal to or higher than 50 Ry. To evaluate the impact of the energy convergence threshold, the equilibrium lattice parameter a_0 is extracted for the three considered values of E_{thr} at fixed cut-off energies of 50 Ry and 80 Ry, as reported in Tab.(2.1) .

E_{thr}(Ry)	a_0 (Å) for E_{cut}=50 Ry	a_0 (Å) for E_{cut}=80 Ry
10^{-6}	4.151842730692	4.151685908399
10^{-9}	4.151841916832	4.151685206026
10^{-12}	4.151841916832	4.151685206026

Table 2.1: Calculated equilibrium lattice parameter a_0 for different energy convergence thresholds E_{thr} at a fixed cut-off energy E_{cut}=50 Ry and E_{cut}=80 Ry.

For both values of E_{cut}, reducing E_{thr} from 10^{-6} Ry to 10^{-9} Ry induces a minor variation in a_0, on the order of 10^{-6} Å; moreover, $E_{thr} = 10^{-9}$ Ry and $E_{thr} = 10^{-12}$ Ry yield lattice parameters that agree to thirteen significant figures. The energy convergence threshold can thus be set to $E_{thr} = 10^{-9}$ Ry. For this value of E_{thr}, the values of a_0 extracted from the fit for different values of E_{cut} are presented in Tab.(2.2).

E_{cut}(Ry)	a_0(Å) for $E_{thr} = 10^{-9}$Ry
40	4.152202031031
50	4.151841916832
60	4.151768294179
70	4.151700737554
80	4.151685206026

Table 2.2: Calculated equilibrium lattice parameter a_0 for different cut-off energies E_{cut} at a fixed energy convergence threshold $E_{thr} = 10^{-9}$Ry.

As shown in Fig.(2.2), the value of the equilibrium lattice parameter calculated for $E_{cut} = 80$ Ry is smaller than the value obtained for $E_{cut} = 40$ Ry by 0.01%; on the other hand, it is smaller than the value attained for $E_{cut} = 50$ Ry by 0.004%. The choice of the cut-off energy E_{cut} seems to have a greater impact on the calculation of the optimal value a_0 than the choice of E_{thr}, as smaller relative variations of E_{cut} lead to greater relative variations of a_0. On account of these considerations, the cut-off energy is set to $E_{cut} = 50$ Ry and the optimal equilibrium lattice parameter is $a_0 = a_{eq}$ =4.1518 Å=7.8458 Bohr; these values, along with $E_{thr} = 10^{-9}$ Ry, are employed in all further scalar-relativistic calculations for bulk gold.

The equilibrium lattice parameter for bulk gold, measured at room temperature (298.15K=25°C), is equal to 4.0786 Å [23]. The calculations reported in this section are ground-state calculations, and thus pertain to a system at temperature T=0K. However, at room temperature, the expansion coefficient is approximately equal to $1.5 \times 10^{-5}\text{K}^{-1}$[23] and decreases with a decrease in temperature; as a result, the difference between the equilibrium lattice parameter at room temperature and at absolute zero is negligible for the purpose of this dissertation and the optimal value a_{eq} of the lattice parameter can be compared to the experimental value at room temperature. The calculated value for a_{eq} exceeds the experimental value at room temperature by approximately 1.8%, which is a satisfactory estimate for the purpose of this thesis; the overestimate of the equilibrium lattice parameter is a well-documented feature of the GGA formalism[24].

In addition to convergence with respect to the cut-off energy, convergence of the total energy with respect to the k-point grid has to be achieved. The previously identified values of E_{thr}, E_{cut}, a_{eq} are fixed and self-consistent calculations of the total energy are performed, varying the number of k-points included in the grid along each direction; due to the cubic symmetry of the FCC lattice, the k-point grid is always chosen in the form $N \times N \times N$. The total energy variation as a function of the number of k-points along each direction is reported in Fig.(2.4).

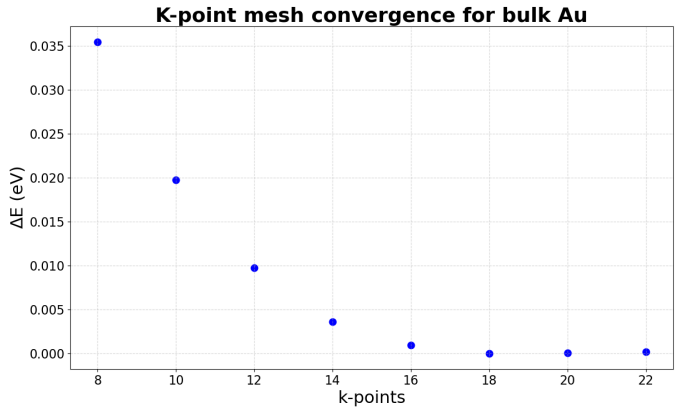

Figure 2.4: Convergence test of the total energy with respect to the k-point grid. Scatter points represent the difference between the total energy - as a function of the number of k-points along each direction in the grid - and its minimum value.

Fig.(2.4) shows that convergence of the total energy is achieved for a $18 \times 18 \times 18$ k-point grid. This k-point grid is employed to sample the first Brillouin zone in all further scalar-relativistic self-consistent calculations for bulk gold.

Essentially equivalent preliminary calculations are carried out for the fully-relativistic case. The Gaussian broadening σ is now set to 0.001 Ry and the energy convergence threshold is fixed to $E_{thr} = 10^{-9}$ Ry from the start; initially, a $18 \times 18 \times 18$ k-point grid is used. The total energies evaluated at each a for varying E_{cut} and their fits are displayed in Fig.(2.5), along with the variation of a_0 with respect to E_{cut}.

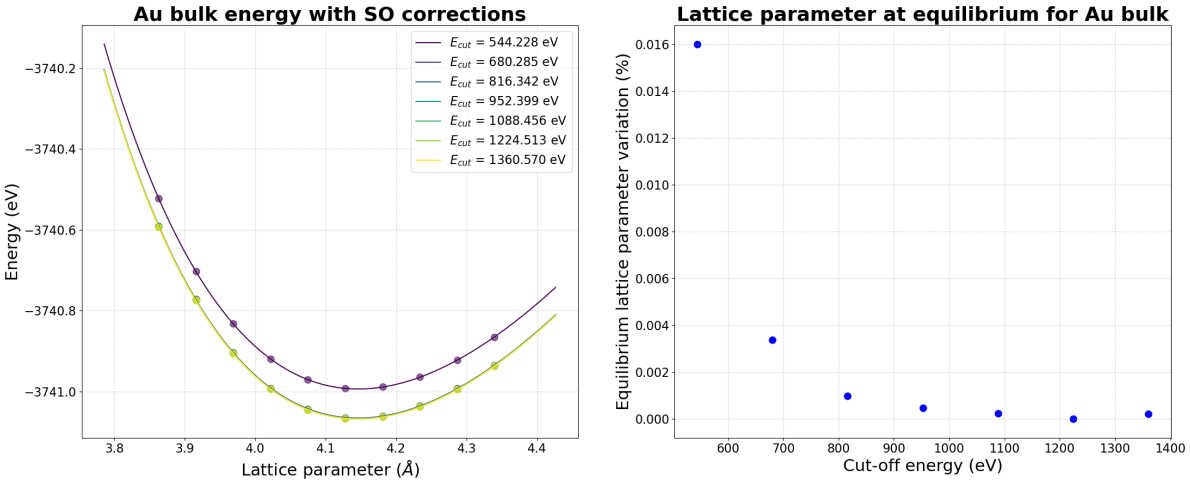

Figure 2.5: Convergence test for the cut-off energy E_{cut} and relative difference between the equilibrium lattice parameter as a function of E_{cut} and its minimum value, at fixed convergence threshold $E_{thr} = 10^{-9}$ Ry $\cong 10^{-8}$ eV, for the fully-relativistic case.

Again, in Fig.(2.5) the total-energy curves drop to lower energies for increasing E_{cut} and are nearly coincident for cut-off energies equal to or higher than 50 Ry. Comparison of Fig.(2.2) and Fig.(2.5) shows that, as expected, the minimum of the total-energy curves in the fully-relativistic calculations is lower than the minimum at the same E_{cut} in the scalar-relativistic case. Furthermore, Fig.(2.5) shows that the value of the equilibrium lattice parameter calculated for $E_{cut} = 50$ Ry exceeds the value attained for $E_{cut} = 80$ Ry by just 0.004%; the cut-off energy is thus set to $E_{thr} = 50$ Ry in all further fully-relativistic calculations for bulk gold, while the employed value of the equilibrium lattice parameter is $a_0 = a_{eq}$=4.1457 Å=7.8342 Bohr. The optimal equilibrium lattice parameter in the fully-relativistic case is smaller than the equilibrium lattice parameter attained in the scalar-relativistic case; therefore, it is a better estimate of the experimental value 4.0786 Å at room temperature. Nonetheless, it exceeds this value by about 1.6%.

The convergence of the total energy with respect to the k-point grid has to be achieved. The previously identified values of E_{thr}, E_{cut}, a_{eq} are fixed in the required self-consistent calculations. The total energy variation as a function of the number of k-points along each direction in the grid is reported in Fig.(2.6).

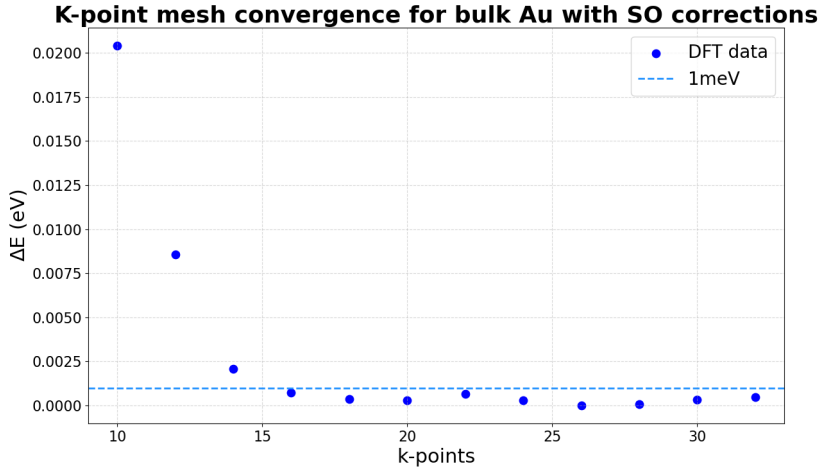

Figure 2.6: Convergence test of the total energy with respect to the k-point grid in the fully-relativistic case. Scatter points represent the difference between the total energy - as a function of the number of k-points along each direction in the grid - and its minimum value. The dashed line is added as a reference for 1 meV.

As shown in Fig.(2.6), the total energy seems to oscillate when increasing the density of the k-point grid; however, since the amplitude of this oscillation is about 1meV, convergence of the total energy is achieved. A $18 \times 18 \times 18$ k-point grid is employed to sample the first Brillouin zone in all further fully-relativistic self-consistent calculations for bulk gold.

2.1.2 Electronic structure of bulk Au

Scalar-relativistic and fully-relativistic calculations of the band structure, density of states and the projected density of states (PDOS) are carried out.

The band structure diagram of a solid represents the energy of the available one-particle electronic states $\epsilon_{n\mathbf{k}} = \epsilon_n(\mathbf{k})$ as a function of the crystal momentum $\mathbf{k}$ in reciprocal space; as $\mathbf{k}$ is a vector, the energy levels are evaluated along a series of lines connecting high-symmetry points in the first Brillouin zone[11], referred to as k-path. For an FCC lattice, the high-symmetry points for the first Brillouin zone are defined in Tab.(2.3), where the primitive vectors of the reciprocal space $\mathbf{b}_i$ (i=1,2,3) are given by Eq.(1.9). The first Brillouin zone of an FFC lattice is represented in Fig.(2.7); moreover, the high symmetry points and the chosen k-path for band structure calculations in this thesis are highlighted.

The band structure diagram is usually paired with the density of states, as defined in Section 1.3, which condenses the properties of the electronic states for all possible wavevectors $\mathbf{k}$ in reciprocal space. The band structure and DOS display the band gaps

$\times\mathbf{b}_1$	$\times\mathbf{b}_2$	$\times\mathbf{b}_3$		$\times\mathbf{b}_1$	$\times\mathbf{b}_2$	$\times\mathbf{b}_3$	
0	0	0	Γ	5/8	1/4	5/8	U
3/8	3/8	3/4	K	1/2	1/4	3/4	W
1/2	1/2	1/2	L	1/2	0	1/2	X

Table 2.3: Symmetry **k**-points of FCC lattice.

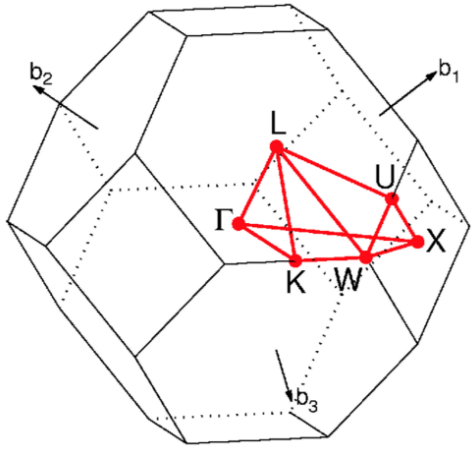

Figure 2.7: Brillouin zone of FCC lattice and high symmetry points (red dots). The k-path Γ-X-W-K-Γ-L-U-W-L-K|U-X is reported (red lines). Image source: Setyawan, Wahyu, and Curtarolo, Stefano. "High-throughput electronic band structure calculations: Challenges and tools." *Computational materials science* 49.2 (2010): 299-312

(allowing the classification of materials as insulators, semiconductors and metals) and offer key insight into allowed electronic transitions and the characteristics of possible magnetic properties.

The scalar-relativistic calculation of the band structure of bulk Au is carried out by performing an initial self-consistent calculation with the computational parameters defined in the previous section, followed by the actual band structure calculation. The latter is a non self-consistent field calculation: it uses the ground-state electron density from the previous step to define the auxiliary Hamiltonian of the system and the Kohn-Sham eigenfunction and eigenvalues are evaluated without updating the Hamiltonian at every iteration. Since spin-orbit effects are now neglected and each band can contain up to two electrons, fifteen energy bands are evaluated in order to have five empty bands. The calculated band structure is reported in Fig.(2.8). A scalar-relativistic band structure diagram[25] from the AFLOW database[26] is used as a reference for qualitative comparison and is reported in Fig.(2.9). It is obtained from DFT calculations using the PAW method in the GGA formalism; 11 valence electrons are considered and a slightly

lower equilibrium lattice parameter is employed.

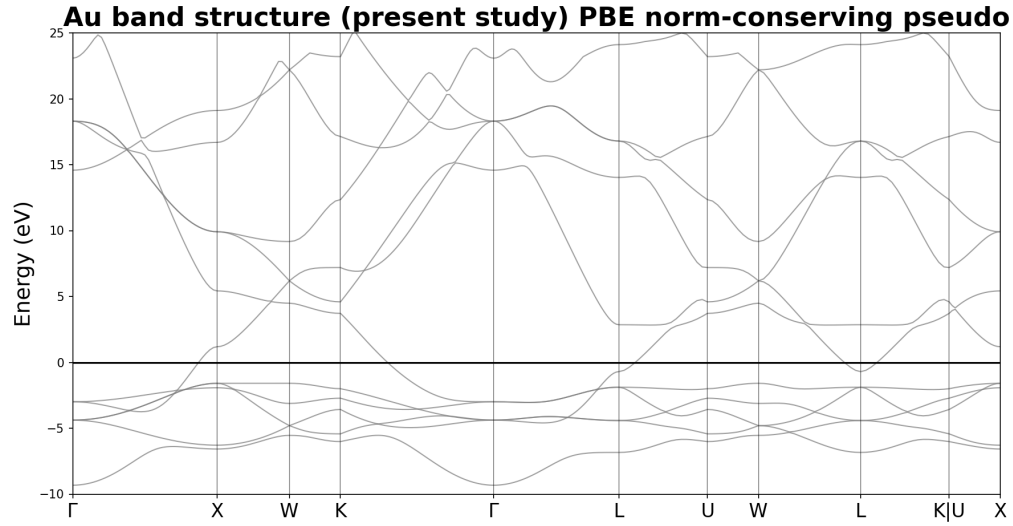

Figure 2.8: Scalar-relativistic band structure. The Fermi energy is set to zero (horizontal gray line).

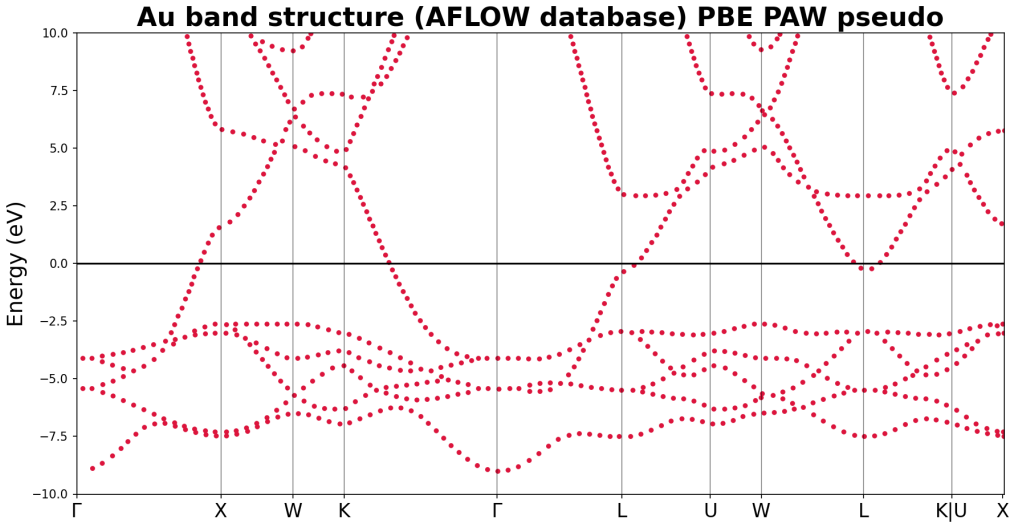

Figure 2.9: Scalar-relativistic band structure from the AFLOW database. The Fermi energy is set to zero (horizontal gray line).

The general behaviour of the bands in the reference along the k-path is reproduced in Fig.(2.8) in the energy range between -10 eV and 10 eV; the small discrepancies in the energy levels can be attributed to the different computational set-up.

An equivalent computation is performed in order to obtain the fully relativistic band structure of bulk Au; as the spin-orbit corrections are now considered, thirty bands are computed (double the number of bands included in the scalar-relativistic calculation). The band structure computed accounting for the spin-orbit corrections is reported in Fig.(2.10) and compared with the result of the scalar-relativistic calculation, reported in light blue.

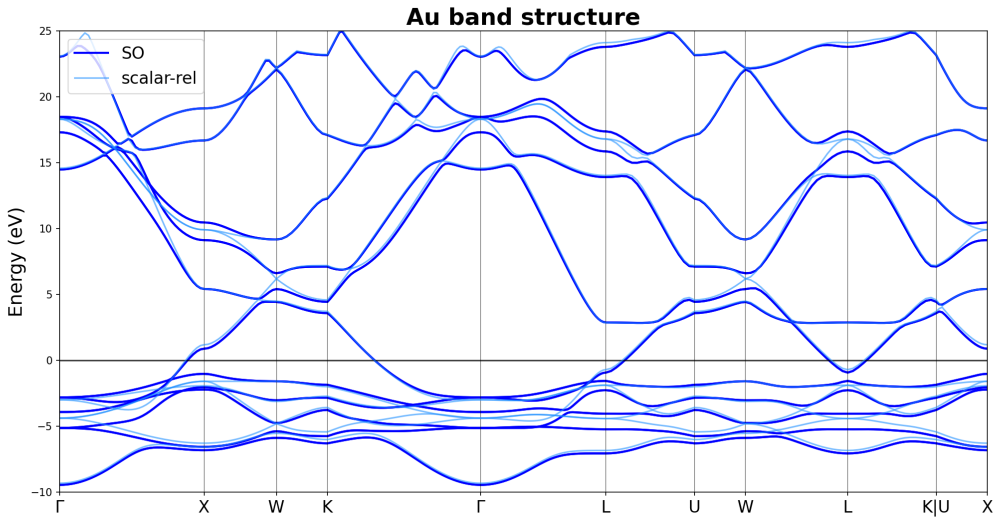

Figure 2.10: Comparison between the fully-relativistic band structure (blue lines) and the scalar-relativistic band structure (faint azure lines). The Fermi energy is set to zero for both diagrams (horizontal gray line).

The inclusion of spin-orbit corrections has the well-known effect of inducing splittings in the energy levels[27]; this is shown in Fig.(2.10), where many of the band crossings in the scalar-relativistic band structure are not visible in the fully-relativistic band structure. Both band structures display flat bands in the energy range between -7.5 eV and the Fermi energy; since the density of states for each band depends on the reciprocal of the energy band gradient in k-space, as Eq.(1.19) shows, comparatively high values of the DOS and a number of Van Hove singularities are expected in this energy range.

The ground-state DOS is computed after a non self-consistent field calculation, which in turn makes use of the ground-state density of a previous self-consistent step. Since the DOS is defined through an integral in the first Brillouin zone, as Eq.(1.19) shows, the

non self-consistent calculation requires a denser k-point grid to attain better accuracy; moreover, if a smearing method is used, the smearing parameter has to be carefully chosen due to its significant influence on the result. The density of states of the system is initially computed in the scalar-relativistic regime, using the Gaussian smearing method. The latter consists in approximating the Dirac delta function $\delta(\epsilon - \epsilon_{n\mathbf{k}})$ in the expression of the DOS

$$g(\epsilon) = \frac{V_{cell}}{(2\pi)^3} \sum_n \int_{B.Z.} \mathrm{d}\mathbf{k}\, \delta(\epsilon - \epsilon_{n\mathbf{k}}), \tag{2.2}$$

with a Gaussian of width σ:

$$\delta(\epsilon - \epsilon_{n\mathbf{k}}) \approx \frac{1}{\sigma\sqrt{\pi}} e^{-\left(\frac{\epsilon - \epsilon_{n\mathbf{k}}}{\sigma}\right)^2}. \tag{2.3}$$

The DOS is calculated varying both the Gaussian broadening σ and the number of k-points in the grid employed in the non self-consistent step; on the other hand, the computational parameters of the initial self-consistent calculation are fixed. The results are respectively reported in Fig.(2.11) and Fig.(2.12).

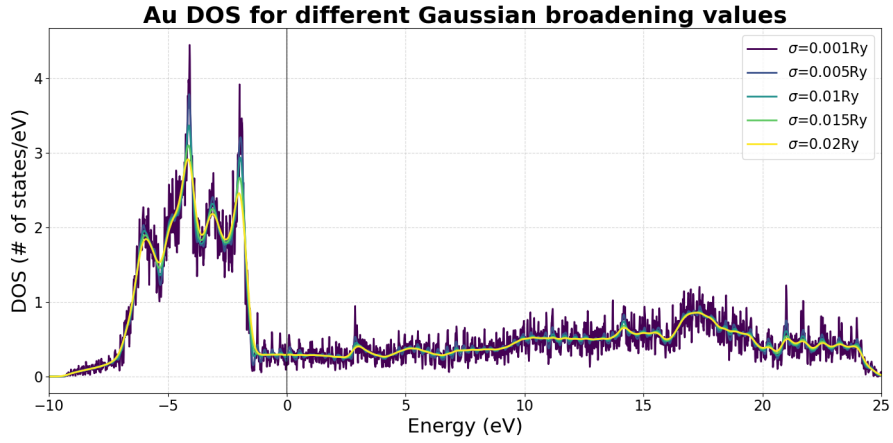

Figure 2.11: Scalar-relativistic DOS obtained by varying the Gaussian broadening σ in the final step of the calculation. The k-point grid in the non self-consistent calculation is a $40 \times 40 \times 40$ mesh. The Fermi energy is set to zero (vertical gray line).

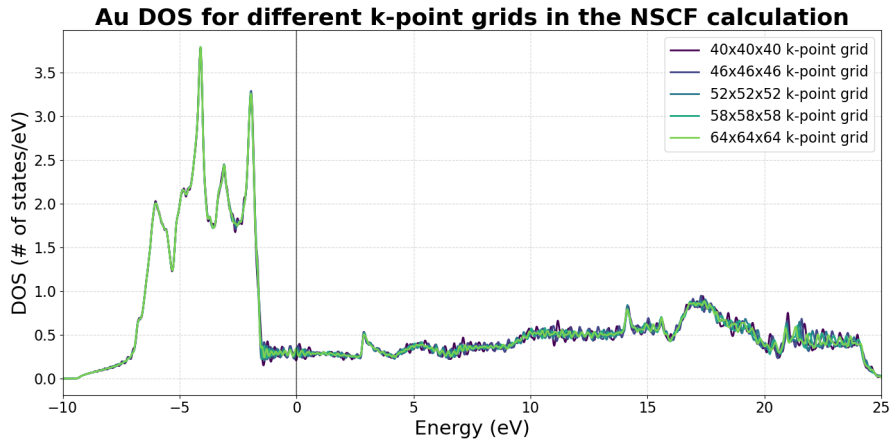

Figure 2.12: Scalar-relativistic DOS obtained by varying the number of k-points in the grid employed in the non self-consistent step. The Gaussian broadening σ in the final step is set to 0,005 Ry. The Fermi energy is set to zero (vertical gray line).

The DOS plot corresponding to the reference band structure[25] from the AFLOW database[26] is used for qualitative comparison; it is reported on the right in Fig.(2.13), along with some of the DOS plots attained in the context of the present study.

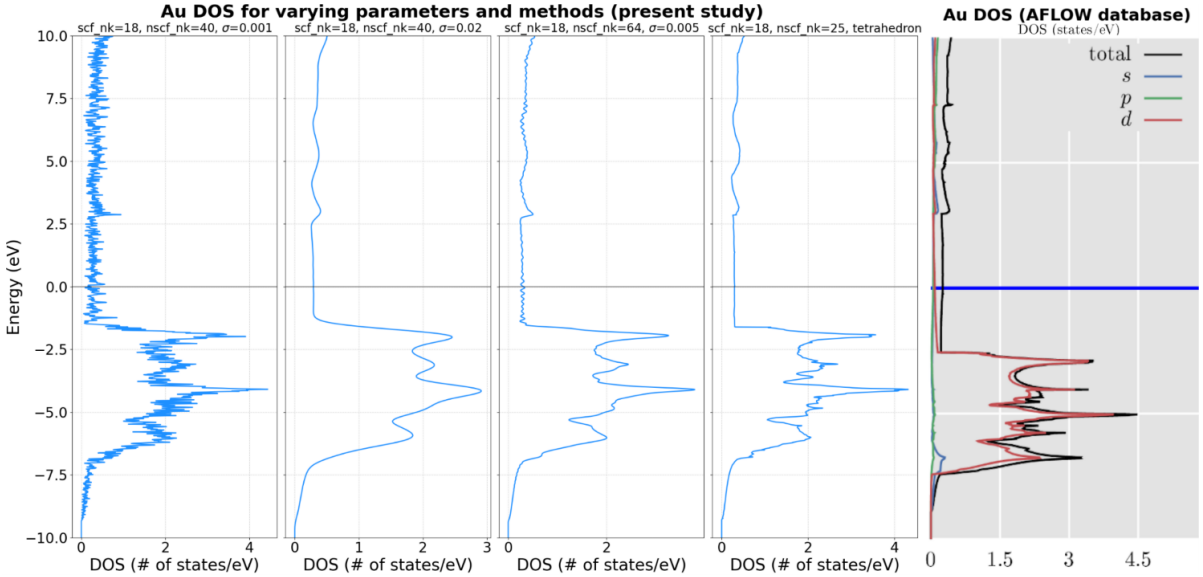

Figure 2.13: Scalar-relativistic DOS of bulk gold. From left to right, the first four plots (azure lines) show the scalar-relativistic DOS attained in the present study for varying parameters and methods. Among these, the first three are calculated employing the Gaussian smearing method, for different densities of the k-point grid in the non self-consistent step and values of the Gaussian broadening. The fourth plot is computed with the tetrahedron method. The plot on the right is retrieved from the AFLOW database[25].

Both in Fig.(2.11) and Fig.(2.12), as expected, the densities of states show prominent and sharp Van Hove singularities in the range between -7.5 eV and -5 eV. However, the DOS for lower values of σ in Fig.(2.11) shows additional, weaker peak structures all over the considered energy range compared to the reference plot; higher values of σ smooth out this spurious noise, but obscure the sharp character of the Van Hove singularities as well. The calculations in Fig.(2.12) reproduce better the stark features of the DOS, but still display weak, artificial peaks compared to the reference plot, even for k-point grids of considerably high density. These characteristics are highlighted through three representative plots in Fig.(2.13). To speed up convergence of the DOS with k-point sampling the tetrahedron method can be used, as it succeeds in reproducing both the sharp peaks and the flat regions in the DOS for comparatively less dense k-point meshes[28]. In the linear tetrahedron method, if an $N \times N \times N$ k-point grid is chosen, the first Brillouin Zone is subdivided into N^3 cubes and each of them is divided into six tetrahedra; within each tetrahedron, the bands are linearly interpolated to approximate the DOS[29]. Convergence of the DOS against the k-point grid is tested, as reported in Fig.(2.14).

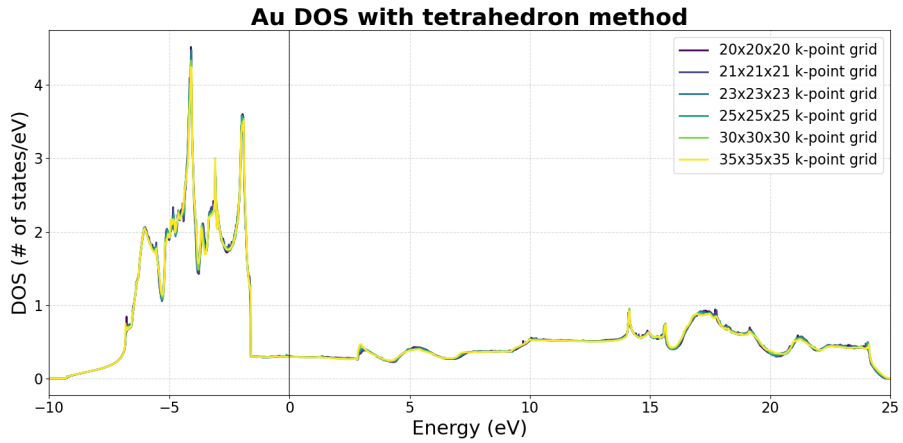

Figure 2.14: Scalar-relativistic DOS obtained by varying the number of k-points in the grid employed in the non self-consistent step. The tetrahedron method is employed. The Fermi energy is set to zero (vertical gray line).

The densities of states in Fig.(2.14) show better qualitative agreement with the reference from the AFLOW database; this is highlighted through a representative plot in Fig.(2.13). Nevertheless, quantitative discrepancies are observed: the prominent structures are shifted toward the Fermi energy with respect to the reference and peak distribution and height are different. This might still be explained by the different computational approach. Given the substantial agreement of the curves in Fig.(2.14), a $21 \times 21 \times 21$ k-point grid is selected for the scalar-relativistic density of states. The fully-relativistic calculation of the density of states is carried out employing the tetrahedron method; the results for the different k-point grids of varying density used in the non self-consistent calculation are presented in Fig.(2.15).

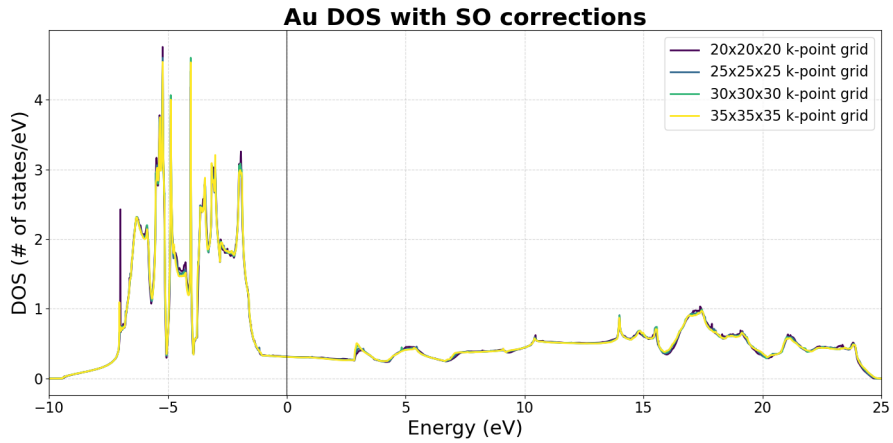

Figure 2.15: Fully-relativistic DOS obtained by varying the number of k-points in the grid employed in the non self-consistent step. The tetrahedron method is employed. The Fermi energy is set to zero (vertical gray line).

The agreement of curves in Fig.(2.15) shows that convergence is reached. Since the curves in Fig.(2.15) essentially agree, a $25\times25\times25$ k-point grid is chosen for the fully-relativistic DOS.

The DOS is then projected onto the atomic orbitals of gold, using the previously defined parameters. The density of states projected onto atomic orbitals (PDOS) or specific atoms reveals information on atomic-level contributions to electronic properties and is used to study bonding, catalysis[30] and doping effects in complex materials[11]. The resulting scalar-relativistic PDOS diagram is reported in Fig.(2.16). Gold is a transition metal; therefore, the electronic configuration of a gold atom features a completely filled 5d sub-shell and a half-filled 6s sub-shell. As expected, the predominant contribution to the density of states below the Fermi level comes from the 5d orbitals, while just above the Fermi energy, the contribution of 6s orbitals becomes more relevant. The projection of the DOS on the 5s orbital is equal to zero over the whole energy range between -10 eV and 25 eV, while 5p orbitals only yield minor contributions; these semicore orbitals yield significant contributions to much lower energies.

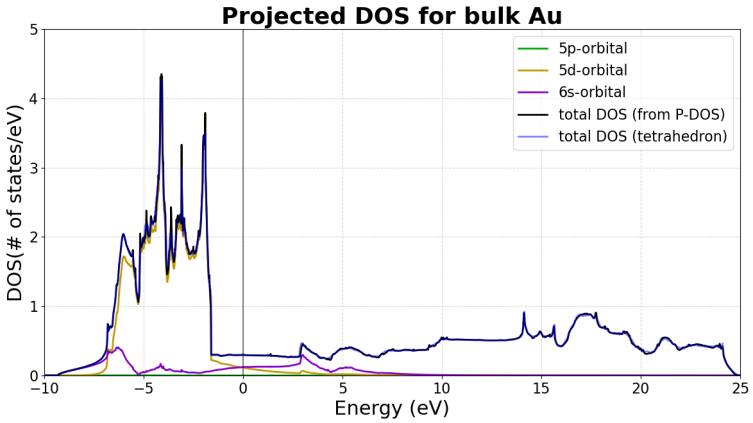

Figure 2.16: Scalar-relativistic PDOS diagram. The tetrahedron method is employed. The Fermi energy is set to zero (vertical gray line).

The projected density of states is computed also including spin-orbit corrections, as reported in Fig.(2.17). As spin-orbit effects are included, all orbital levels, except for the s orbitals, are split into two sublevels, labelled by the quantum number $j = l \pm \frac{1}{2}$; l is the electron orbital quantum number and $\frac{1}{2}$ is the electron spin quantum number. Just as in the scalar-relativistic case, the density of states is dominated by 5d orbitals below the Fermi level, in the energy range between -7 eV and -1 eV . At lower energies (approximately between -7 eV and -5 eV) the contributions from the 5d orbitals (l= 2) with $j = \frac{3}{2}$ are more relevant, whereas contributions from the 5d orbitals with $j = \frac{5}{2}$ are dominant closer to the Fermi energy; the fact that the lower value of j is associated with the lower energies is consistent with the theory of spin-orbit coupling. In the single-electron picture, the spin-orbit correction to energy levels depends on a factor $\frac{\xi}{2}[j(j+1) - l(l+1) - \frac{1}{2}(\frac{1}{2}+1)]$, where ξ is the spin-orbit coupling constant; for 5d orbitals, this factor is negative if $j = \frac{3}{2}$ and, on the contrary, positive if $j = \frac{5}{2}$, yielding a downward shift in the energy of the$j = \frac{3}{2}$ states and an upward shift of the $j = \frac{5}{2}$ states[31].

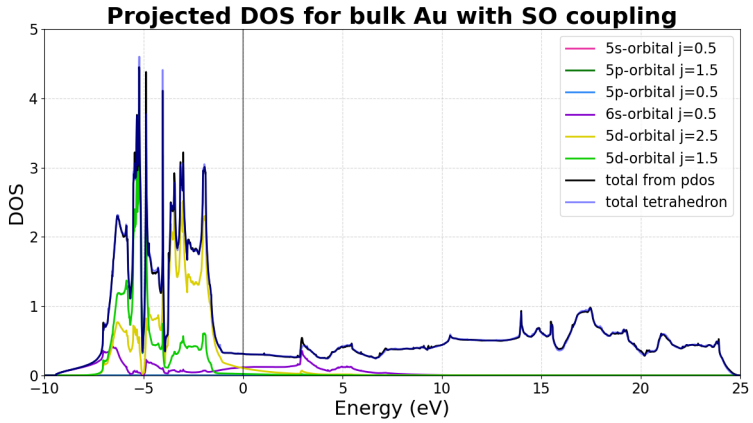

Figure 2.17: Fully-relativistic PDOS diagram. The tetrahedron method is employed. The Fermi energy is set to zero (vertical gray line).

The DOS calculated using the tetrahedron method, respectively in the scalar-relativistic and in the fully-relativistic regime, is presented next to the corresponding band structure in Fig.(2.18) and in Fig.(2.19), in order to highlight the correspondence between sharp and prominent peaks in the density of states and the flat valence bands. The diagrams reveal that the band splitting induced by the inclusion of spin-orbit corrections leads to a more peaked DOS below the Fermi energy.

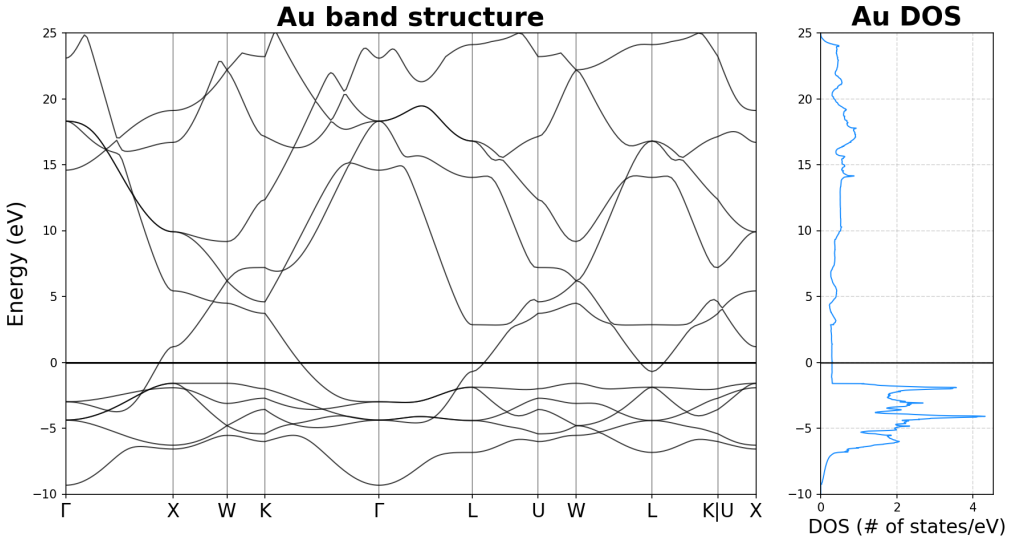

Figure 2.18: Scalar-relativistic band structure (gray lines) and density of states (azure line). The Fermi energy is set to zero for both diagrams (horizontal black line).

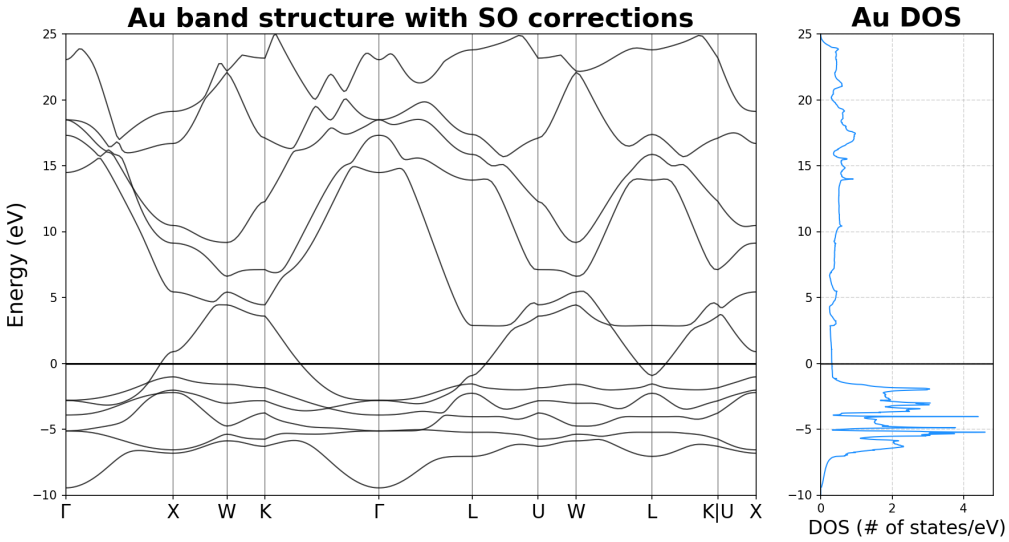

Figure 2.19: Fully-relativistic band structure (gray lines) and density of states (azure line). The Fermi energy is set to zero for both diagrams (horizontal black line).

Fig.(2.16) and Fig.(2.17) show that the flat, fully occupied bands just below the Fermi energy are essentially of 5d-character. A key characteristic of the band structure of gold is the energy separation between its topmost filled 5d-character band and the partially filled 6sp conduction band that crosses the Fermi level, as it governs the optical properties of gold [32]; this energy difference is strongly dependent on the k-point. The regions around X and L in the first Brillouin zone are particularly relevant, as they correspond to the smallest energy gaps between the topmost occupied d-band and the empty states of the conduction band above the Fermi level. The energy difference between the Fermi energy and the topmost occupied d-band at k-points near X is known to be roughly $E_X \approx$1.8 eV, whereas near L it is approximately $E_L \approx$ 2.4 eV; the role of these energy values in the optical absorption of gold will be clarified in Section 2.1.3. The computed band structure in the scalar-relativistic case yields the values $E_X \approx$1.8 eV and $E_L \approx$1.9 eV. While the energy separation near point X is correctly reproduced, near point L it is underestimated by 0.5 eV. Indeed. DFT calculations, within the generalized-gradient approximation, usually yield an underestimation of the energy gap between the topmost filled 5d-character band and the partially filled 6sp conduction band on the order of 1 eV, as documented in literature[33]. As displayed in Fig.(2.10), the introduction of spin-orbit corrections causes the topmost completely filled 5d band to be closer to the Fermi level at point X, leading to a further underestimation: while the energy gap near L is still $E_L \approx$1.9 eV, near point X it reduces to $E_X \approx$1.1 eV.

2.1.3 Optical properties of bulk Au

The optical absorption spectrum of bulk gold is calculated in the long-wavelength limit, with incoming radiation oscillating with frequency ω and characterized by a small wavevector $\mathbf{q}$ ($\mathbf{q} \to 0$ limit). Simulations are carried out either at the independent-particle RPA level (IP-RPA) or including local field effects (LFE-RPA).

The absorption of light by bulk gold depends on both interband and intraband transitions between electronic states[34]. Interband transitions are quantum-mechanical excitations from an occupied state below the Fermi level to an unoccupied state in a higher band upon the absorption of a photon, while intraband transitions result from excitations of electrons into a higher energy level within the same band. The two occur in different energy ranges.

In bulk gold, the main interband contributions to optical absorption are yielded by electron transitions between the fully occupied 5d bands, associated to prominent values of the DOS and Van Hove singularities, and the conduction band above the Fermi level; in particular, interband absorption in the visible range takes place from the topmost occupied d-band to states just above the Fermi energy.

As previously mentioned, the smallest energy gaps between the topmost occupied d-band and the empty states above the Fermi level are found near high-symmetry points X and L in the first Brillouin zone and indeed the optical response of bulk gold is governed by the band structure in these regions[32]. The interband gap between the topmost d-band and the Fermi level near X, $E_X \approx 1.8$ eV (red light wavelength, $\lambda = 688.8$ nm), is the threshold for interband contributions; furthermore, at the analogous energy separation near L, $E_L \approx 2.4$ eV (below green light wavelength $\lambda = 516.6$ nm), interband transitions show a steep onset[34].

Importantly, this sharp absorption edge, causing strong absorption of blue and violet light, explains the yellow color of gold. As well documented in literature, the location of the onset in absorption is due to relativistic effects, which cause the atomic 5d orbitals to rise in energy and the 6s orbital to be lowered in energy; this leads to the shift of absorption from ultraviolet to lower energies in the blue visible range [35]. As gold is a heavy atom (Z=79), relativistic effects are intense: gold thus displays a characteristic color that distinguishes it from most metals, even those that share its electronic configuration (e.g. Ag, Z=47).

Intraband processes in bulk gold involve electrons in the partially filled conduction band and dominate the optical response at photon energies in the infrared range, below the threshold $E_X \approx 1.8$ eV. For near-infrared wavelengths, gold behaves like a free-electron gas and can thus be described by the Drude model[32]; the dielectric function in the Drude model has the expression

$$\epsilon^f_{\mathrm{mac}}(\omega) = 1 - \frac{\omega_D^2}{\omega^2 + i\gamma\omega}, \tag{2.4}$$

where ω_D is the plasma frequency for gold and γ is the electron relaxation rate.

IP-RPA optical properties of bulk Au

The optical absorption spectrum of bulk gold in the $\mathbf{q} \to 0$ limit is calculated employing the YAMBO code; these calculations rely on the generation of a database from a non self-consistent calculation carried out using Quantum ESPRESSO. YAMBO computes the optical absorption spectrum from first principles through Eq.(1.62): the macroscopic dielectric function is obtained as reported in Section 1.5.2, starting from the solution of the Dyson-like Eq.(1.55) for the susceptibility $\chi_{\mathbf{GG'}}(\mathbf{q}, \omega)$ in the random phase approximation.

As the FCC lattice yields isotropic optical properties, the direction of the incoming wavevector $\mathbf{q}$ does not influence the results for bulk Au. The scalar-relativistic band structure calculation in the previous section yielded the energy separations $E_X \approx 1.8$ eV and $E_L \approx 1.9$ eV; therefore, the absorption spectrum is expected to display a prominent onset at 1.9 eV, just above the threshold for interband contributions $E_X \approx 1.8$ eV.

At first, LFE are neglected. A convergence test of the imaginary part of the dielectric function at the IP level against the number of bands included in the non self-consistent calculation is carried out; the results are shown in Fig.(2.20). A $40 \times 40 \times 40$ k-point grid is employed in the non self-consistent step and the YAMBO damping parameter is set to 0.1 eV. A phenomenological Drude term, as defined in Eq.(2.4), is added to the dielectric function to account for intraband transitions; the relaxation energy is set to $\hbar\gamma$ =0.1 eV, as suggested in Ref.[36], while the Drude energy is set to the value $\hbar\omega_D$=8.48 eV, taken from Ref.[37].

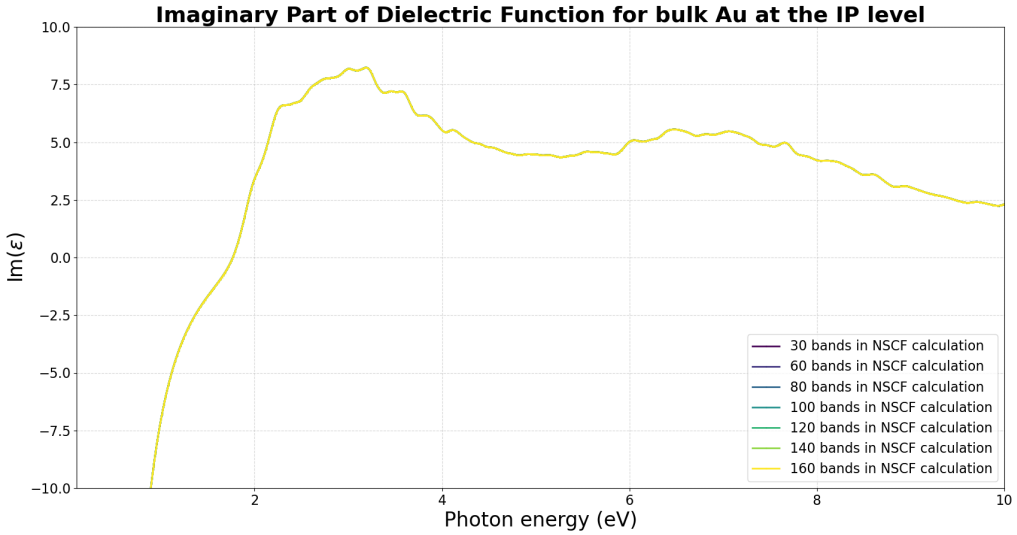

Figure 2.20: Convergence test of the imaginary part of the dielectric function at the independent-particle level against the number of bands included in the calculation.

All curves in Fig.(2.20) overlap, therefore for further optical properties calculations of bulk Au, the number of included bands is set to 30. However, the absorption spectrum shows anomalous behaviour below 1.8 eV -the expected threshold for interband contributions- as it takes non-physical negative values and eventually diverges to $-\infty$ when photon energy tends to zero. Due to this unresolved anomaly, the Drude term is not included and intraband contributions are neglected throughout this thesis in all YAMBO calculations.

Subsequently, convergence of the imaginary part of the dielectric function at the IP level with respect to the k-point mesh in the non self-consistent calculation is tested. To ease convergence, the damping parameter is increased to 0.15 eV. The attained absorption spectra are reported in Fig.(2.21).

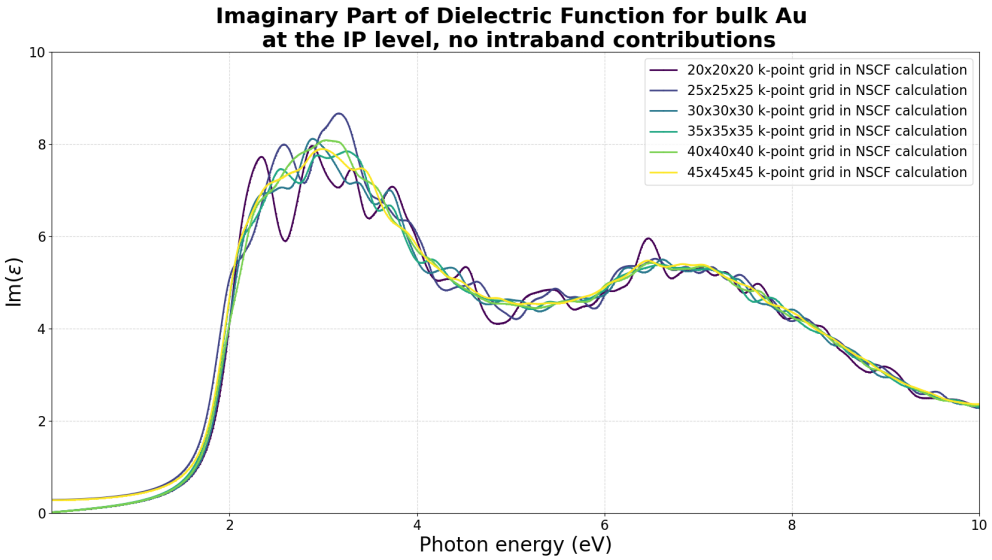

Figure 2.21: Convergence of the imaginary part of the dielectric function at the IP level against the k-point grid employed in the non self-consistent calculation; intraband contributions are neglected.

The absorption profiles attained from the $40\times40\times40$ and $45\times45\times45$ k-point grids show residual fluctuations but are close in the whole considered energy range; although full convergence is not strictly achieved, the $40\times40\times40$ k-point grid is selected for further calculations (unless otherwise specified). It is noteworthy that the absorption spectra in Fig.(2.21) display a steep rise around 2 eV, in agreement with the value E_L ≈1.9 eV of the energy separation between the Fermi level and the topmost occupied 5d band near L, yielded by the scalar-relativistic calculation of the band structure.

LFE-RPA optical properties of bulk Au

Local field effects are included in the calculation of the imaginary part of the dielectric function. A careful convergence test has to be performed with respect to the parameter denoted as "response block size", which is an energy cut-off that determines the number of reciprocal lattice vectors included in the calculation of the susceptibility $\chi_{\mathbf{GG'}}(\mathbf{q},\omega)$, and thus the size of the dielectric matrix in $\mathbf{G}$-space. The convergence test is carried out on spectra built on a non self-consistent calculation where a $20\times20\times20$ k-point grid is used, in order to keep computational costs low; the results are shown in Fig.(2.22).

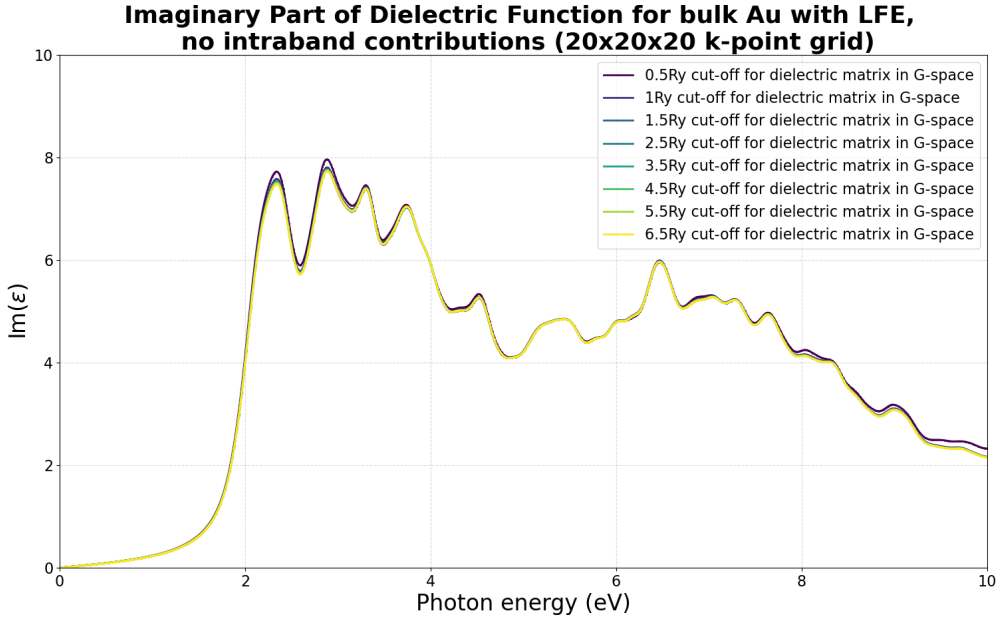

Figure 2.22: Convergence of the imaginary part of the dielectric function including local field effects against the energy cut-off for the dielectric matrix in **G**-space; intraband contributions are neglected.

The absorption spectra essentially overlap for all response block size values beyond 0.5 Ry, therefore an energy cut-off equal to 1.5 Ry is chosen. As this value is automatically adjusted by YAMBO to 2 Ry, the response block size is set to 2 Ry in dielectric-function calculations including LFE.

Finally, the imaginary part of the dielectric function considering LFE is evaluated with the computational parameters identified in this section; it is reported in light blue in Fig.(2.23) and compared to the imaginary dielectric function at the IP level. The inclusion of LFE leads to slight discrepancies between the two spectra, which almost coincide over the whole energy range between 0 and 10 eV. This agrees with the idea that local field effects reflect inhomogeneity at the microscopic scale, so that the highly symmetric and close-packed FCC lattice[2] yields minor local field effects, and bulk gold is homogenous and isotropic at the macroscopic scale.

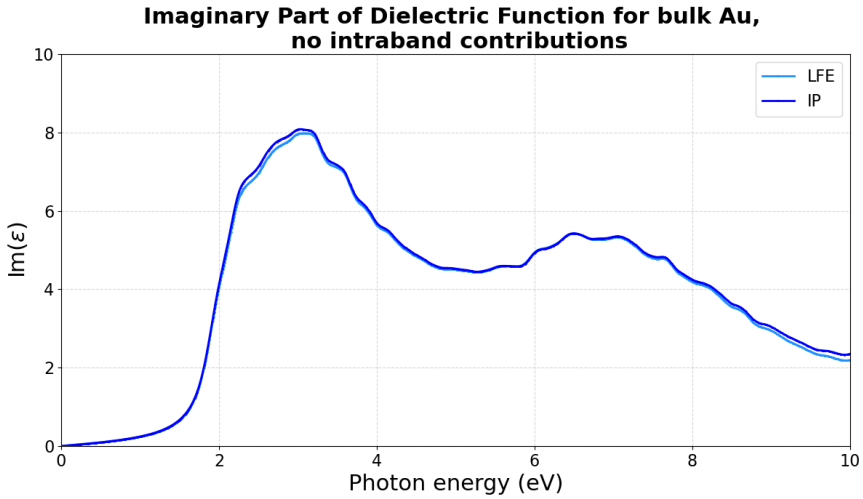

Figure 2.23: Comparison between the imaginary part of the dielectric function for bulk gold in the random phase approximation attained at the IP level (blue line) and including local field effects (azure line).

The absorption spectrum of bulk gold is finally compared to experimental data at room temperature[38] and to a previous DFT calculation of the imaginary part of the dielectric function within the random-phase approximation[39], both presented in Fig.(2.24). The latter was obtained employing the SCAN exchange-correlation functional, a numeric atomic orbital basis set and an *ab initio* lattice parameter equal to 4.084 Å.

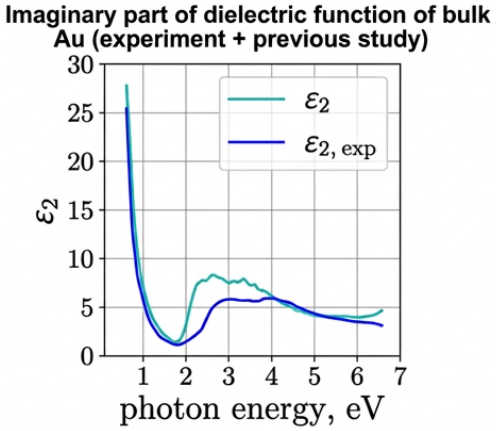

Figure 2.24: Imaginary part of the dielectric function, indicated as ε_2. The experimental data from Ref.[38] is reported (blue line) along the absorption spectra computed in Ref.[39](light blue line). Image source: Maria K Pogodaeva *et al* 2021 *J. Phys.: Conf. Ser.* 1890 012008

The relevance of the contribution of intraband transitions to optical absorption is visible in Fig.(2.24): the experimental absorption spectrum at low energies -below 1.8 eV- shows a tail that diverges as energy tends to zero, well reproduced by the calculation from Ref.[39], where a Drude term with parameters calculated from first principles was added. In the calculation attained in this section, as expected, the onset of the imaginary part of the dielectric function occurs at lower photon energy than in the experimental spectrum, where it is located around 2.4 eV. Furthermore, it fails to reproduce the shape of the main peak, located above 2 eV, and overestimates its height by a few units. However, the absorption spectrum of the present study shows a similar behaviour to the calculated spectrum of Ref.[39] in the energy range between 2 eV and 6 eV; the maximum value for both plots in this energy range is around 8 and the absorption edge is found around 2 eV.

2.2 Au(111) surface

Building upon the results attained for bulk gold, this section investigates the ground-state electronic structure and the optical properties of the Au(111) surface through first-principle slab calculations. All electronic-structure simulations are carried out using the Quantum ESPRESSO integrated suite[18][19]. Several Au(111) slabs with different thickness are generated through the ASE library[40], employing the equilibrium lattice parameter calculated in the scalar-relativistic regime. The surface energy is then computed. Furthermore, the DOS and layer-resolved PDOS are calculated for Au(111) slabs with varying thickness. Finally, the YAMBO code[20][21] is used to compute the optical absorption spectrum of different slabs within the random phase approximation, both at the IP level and including local field effects. The scalar-relativistic pseudopotential employed in all calculations was generated using the ONCVPSP (Optimized Norm-Conserving Vanderbilt PSeudopotential) code[22] and includes 19 valence electrons. The PBE exchange-correlation functional[10] is employed.

2.2.1 Surface modelling and surface energy

First-principle calculations play a crucial role in determining surface properties, as the study of such systems through experimental means entails great challenges[41]. Since surfaces break the periodicity of crystalline solids, it is not possible to directly define a 3D unit cell as done for bulk calculations. The standard procedure for plane wave codes is to build a periodic stack of slabs, which represent two-dimensional thin films that are oriented to expose the surface of interest to vacuum. This is achieved by creating unit cells that are composed of a stack of a finite number of layers -each including a finite number of atoms- and an upper and lower vacuum region in the stacking direction. Assuming the stacking direction to be parallel to the z axis, when 3D boundary

conditions are applied, such a unit cell yields a system composed of periodic images of a slab that is perpendicular to the z axis and extends infinitely in the x-y plane. A schematic representation of the slab model is illustrated in Fig.(2.25). The slab should

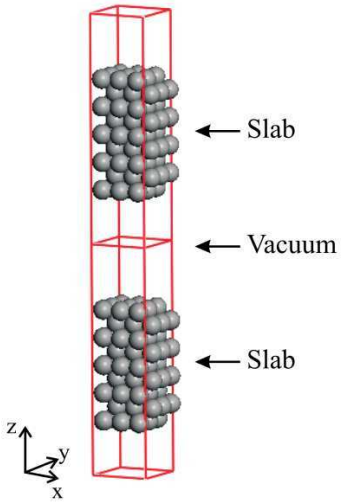

Figure 2.25: Schematic illustration of the periodic stack of slabs generally used to model surfaces. Two unit cells are highlighted (red lines). Image source: Jolayemi, Omamuyovwi " Electronic and surface properties of molybdenum: a first principle study." *Journal of Nigerian Association of Mathematical Physics* 39 (2017).

be thick enough that there is no interaction between opposite surfaces and the vacuum distance between slabs should guarantee that there is no interaction between adjacent replicas. Furthermore, the position of the atoms in the unit cell should reflect surface relaxation, which is the process of variation of the interlayer distance at the facet: atoms spontaneously rearrange in a more energetically favourable configuration at the surface to minimize the instability caused by dangling bonds.

In order to study the electronic structure of the (111) surface of gold, unit cells for slabs of thickness varying between 2 and 10 atomic layers are generated employing the scalar-relativistic equilibrium lattice parameter identified in Section 2.1.1; the stacking direction is parallel to the z axis. Each layer contains a single gold atom. The thickness of the upper and lower vacuum regions is set to 10 Å. The primitive lattice vectors defining the unit cell that lie in the x-y plane, $\mathbf{a}_1$ and $\mathbf{a}_2$, have fixed magnitude; the norm of the third primitive lattice vector $\mathbf{a}_3$, parallel to the stacking direction, obviously increases with increasing slab thickness.

A calculation for structural relaxation is then performed on all slabs: the self-consistent solution of the Kohn-Sham equations is paired with the optimization of the slab geometry, allowing atomic positions -but not the lattice constant- to vary until force convergence is achieved. The cut-off energy, the energy convergence threshold and

the equilibrium lattice parameter are those identified in Section 2.1.1. The Marzari-Vanderbilt smearing method is used and the smearing parameter is set to 0.001 Ry. The convergence threshold for forces is set to 10^{-4}Ry/Bohr. It is important to note that a $18 \times 18 \times 1$ k-point grid is used. In the slab model for an FCC crystal, the magnitude of the primitive vector $\mathbf{a}_3$, parallel to the stacking direction, is considerably longer compared to the magnitude of $\mathbf{a}_1$ and $\mathbf{a}_2$; this is due to the inclusion of layers and vacuum. The corresponding reciprocal lattice primitive vector $\mathbf{b}_3$ is thus shorter than the others, leading to a narrow Brillouin zone in that direction; moreover, the inclusion of large vacuum regions in the unit cell causes the electron density to rapidly tail off to zero at the slab edge. This entails that one k-point is sufficient to sample the Brillouin zone in the stacking direction[11].

Subsequently, the formation energy of a surface is extracted from slab calculations. Indeed, the surface energy E_{surf} is given by the following limit

$$E_{surf} = \lim_{N\to\infty} \frac{1}{2}(E^N_{slab} - NE_{bulk}), \tag{2.5}$$

where E^N_{slab} is the total energy of a N-layer slab and E_{bulk} is the total bulk energy per atom, attained from a different calculation[42]. This expression isolates the surface contribution to the total energy of an infinite slab; the factor $\frac{1}{2}$ accounts for the two surfaces of the slab. In practice, slabs of finite thickness are chosen for calculations and the convergence of surface energy should be tested increasing the number of atomic layers. However, if there is any discrepancy between E_{bulk} and the change in E^N_{slab} with the addition of a layer, the calculated surface energy diverges linearly with N. Fiorentini and Methfessel thus proposed a different technique to extract convergent surface energies from slab calculations[42]. The definition of E_{surf} implies that, when convergence is approached, E^N_{slab} shows a straight line behaviour

$$E^N_{slab} \approx 2E_{surf} + NE_{bulk}, \tag{2.6}$$

already dominant at low slab thickness. Surface energy can then be taken as half the intercept of the linear fit of E^N_{slab} as a function of N, as Eq.(2.6) shows. The Fiorentini-Methfessel method is employed here to extract the surface energy of the gold (111) surface, as reported in Fig.(2.26). Total energies are collected from structural relaxation.

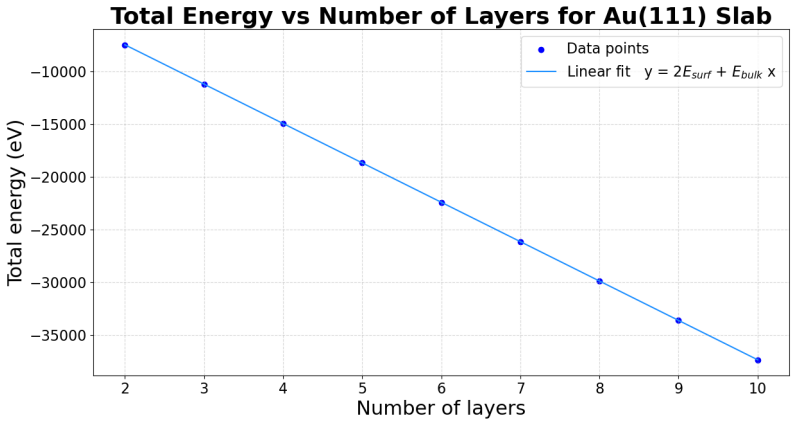

Figure 2.26: Linear fit of the total slab energy as a function of slab thickness.

Fig.(2.26) exhibits the linear behaviour of the total energy of the slabs against the number of layers. The surface energy E_{surf}=0.3523 eV is extracted from the fit; divided by the area of the rhombic (111) surface unit cell, it yields the surface energy per unit area σ_{surf} =0.04733 eV/Å^2.

To evaluate the convergence of the surface energy, the linear fit is performed on expanding sets of slabs; the convergence test is reported in Fig.(2.27). Specifically, the surface energy is calculated by fitting the total energies of all slabs from 2 layers up to 4 layers at first, then of slabs from 2 up to 5 layers and so forth. Convergence is achieved for the set including all slabs from 2 up to 8 layers, but the surface energy is well reproduced by the linear fit on the set including slabs from 2 up to 6 layers.

2.2.2 Electronic structure of the Au(111) surface

The ground-state density of states is computed for all the generated Au(111) slabs, except for the 7-layer slab, as its geometry failed to converge in the relaxation calculation. The non self-consistent step is performed employing the previously identified parameters; convergence of the DOS against the k-point grid used in the non-self consistent step is carried out on the 6-layer slab. Two representative DOS diagrams are shown in Fig.(2.28). The DOS reported in purple is yielded by a $51 \times 51 \times 1$ k-point grid, the most dense mesh employed in the convergence test; the DOS reported in yellow is yielded $39 \times 39 \times 1$ k-point grid. The latter is selected because, even though it leads to the overestimation of height some peaks, it captures the overall behaviour of the DOS and ensures lower computational costs. The identified $39 \times 39 \times 39$ k-point mesh is used in the calculation of the DOS of all slabs.

The DOS for varying slab thickness, normalized to the number of atoms in the slab unit cell, is presented in Fig.(2.29); the scalar-relativistic DOS for bulk gold is reported

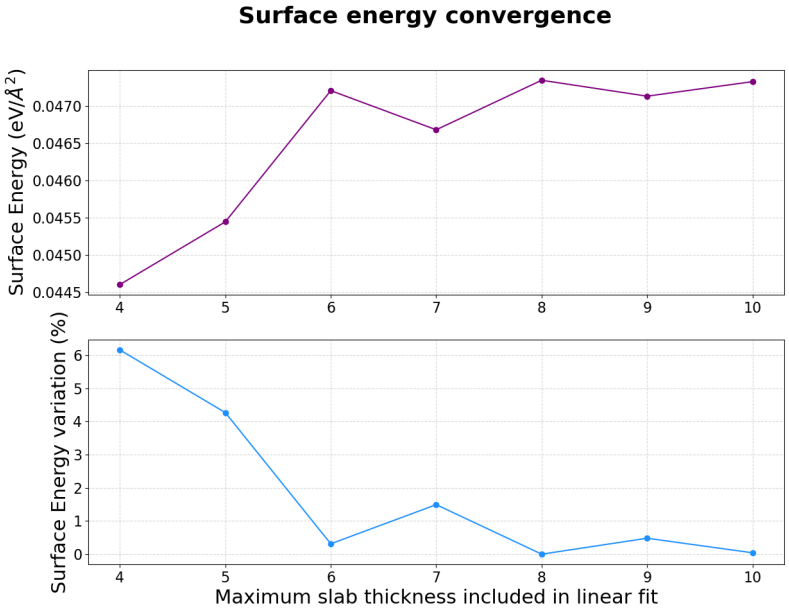

Figure 2.27: Surface energy as a function of the maximum slab thickness included in the linear fit (upper plot). Each point is obtained through a fit performed on a progressively larger dataset. The relative variation with respect to the surface energy attained from the largest slab set (lower plot).

in black for comparison. The densities of state are more structured than the bulk DOS, with more pronounced peaks and Van Hove singularities. This is especially noticeable below the Fermi level, in the energy range between -7.5 eV and -1.2 eV, and in the energy range between 5 eV and 12 eV, corresponding to unoccupied states.

As slab thickness increases, the overall behaviour of the curves tends to reproduce the bulk DOS. For instance, the DOS of the 2-layer slab below the Fermi energy is more localized than the bulk DOS and shows more prominent peaks, while the DOS of the 10-layer slab is in good qualitative agreement with the bulk DOS, although it is more peaked. Furthermore, as illustrated in Fig.(2.30), the densities of state of the Au(111) slabs at low energies (approximately in the range between -9.4 eV and -7.4 eV) display the typical staircase structure of the DOS in quantum wells with infinite barriers[43]. This effect can be attributed to quantum confinement of the electrons in the z direction, due to the finite slab thickness and to the inclusion of vacuum, effectively confining them as quantum wells with infinite barriers. The Au(111) slabs composed of two, five and ten atomic layers are selected for further electronic-structure calculations and optical-properties calculations.

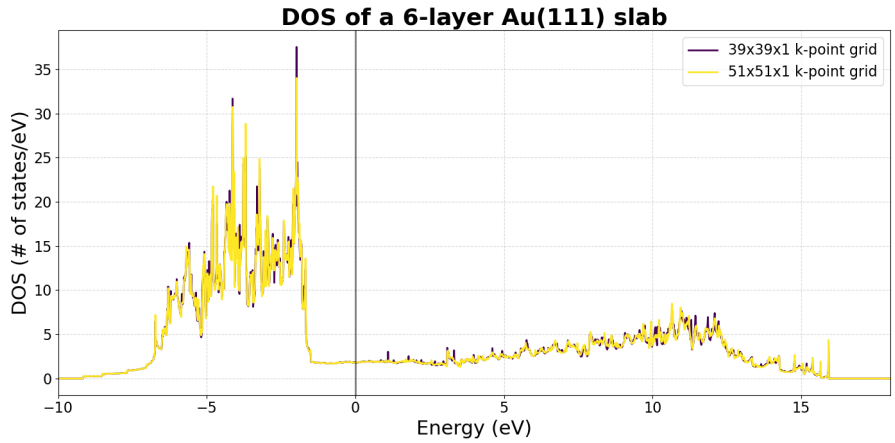

Figure 2.28: Representative DOS plots from the convergence test against the k-point grid used in the non self-consistent step: one is attained from a $39 \times 39 \times 1$ k-point grid(purple line), the other from a $51 \times 51 \times 1$ k-point grid(yellow line). The Fermi energy is set to zero (vertical gray line).

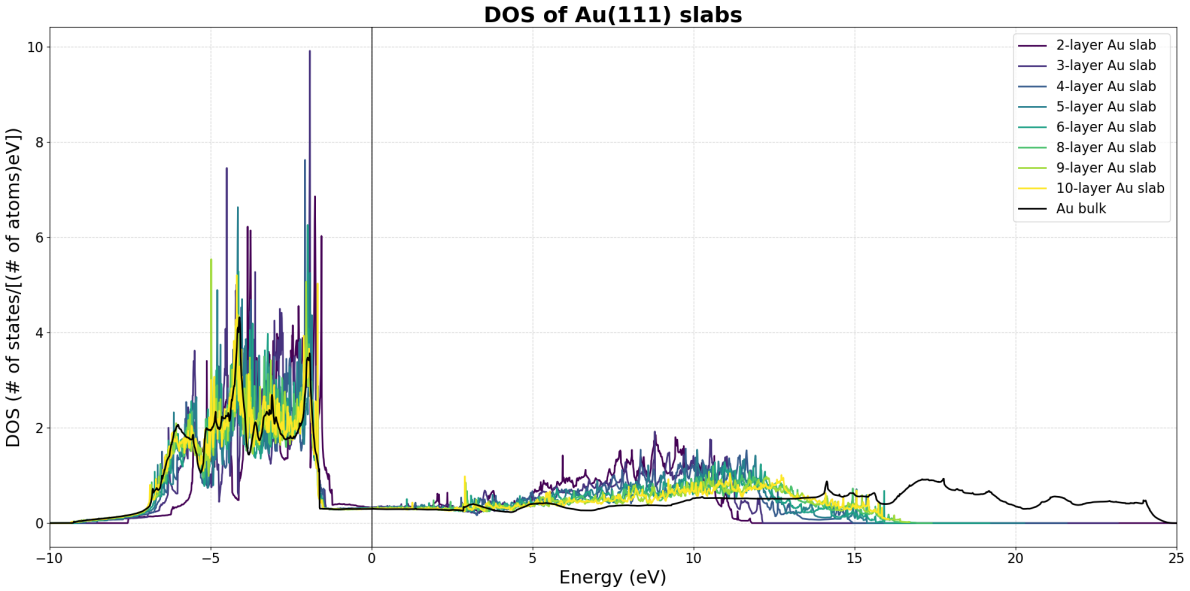

Figure 2.29: Density of state diagrams for Au(111) slabs of varying thickness. The DOS of bulk gold is added as a reference (black line). The Fermi energy is set to zero for all diagrams (gray vertical line).

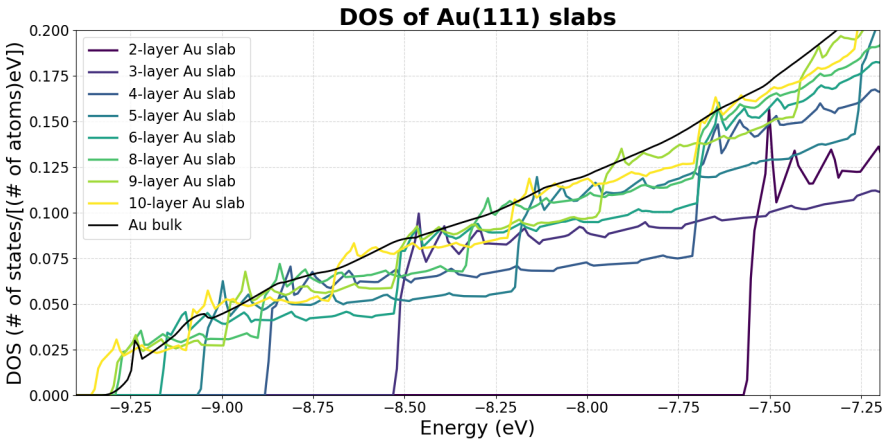

Figure 2.30: Detail of the density of state diagrams for Au(111) slabs of varying thickness. The DOS of bulk gold is added as a reference (black line).

Au(111) projected and layer-resolved DOS

The density of states is then projected onto the atomic orbitals of gold and onto each individual atom in the unit cell. The layer-resolved DOS of the 2-layer, 5-layer and 10-layer slabs projected onto the 5d orbitals is respectively shown in Fig.(2.31), Fig.(2.32) and Fig.(2.33) and compared with the bulk PDOS of the 5d orbitals. While the $39\times39\times1$ k-point grid in the non self-consistent step is adequate for the 2-layer and 5-layer slabs, the calculation for the 10-layer slab is performed using a $47 \times 47 \times 1$ k-point grid, in order to eliminate spurious peaks at the band edge.

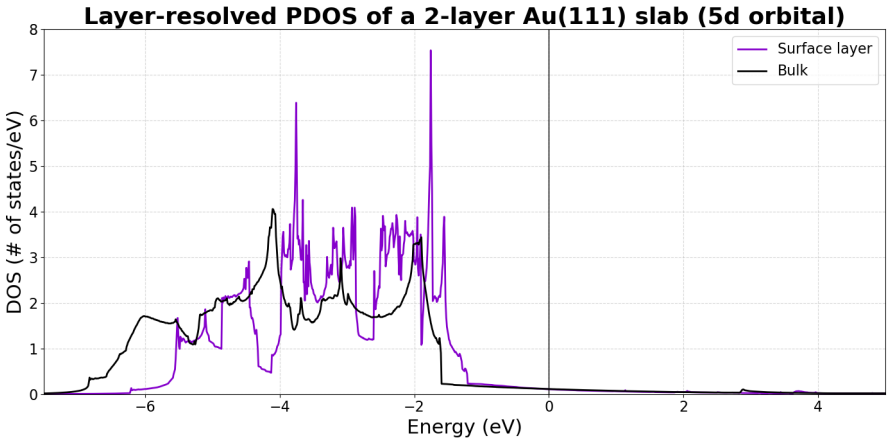

Figure 2.31: Layer-resolved PDOS of 5d orbitals of the 2-layer Au(111) slab. The bulk PDOS of the 5d orbital is added as a reference (black line). The Fermi energy is set to zero for all plots (gray vertical line).

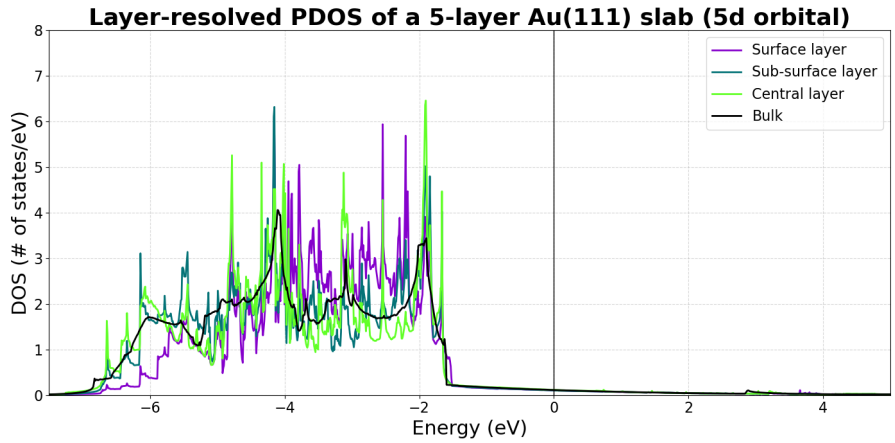

Figure 2.32: Layer-resolved PDOS of 5d orbitals of the 5-layer Au(111) slab. The bulk PDOS of the 5d orbital is added as a reference (black line). The Fermi energy is set to zero for all plots (gray vertical line).

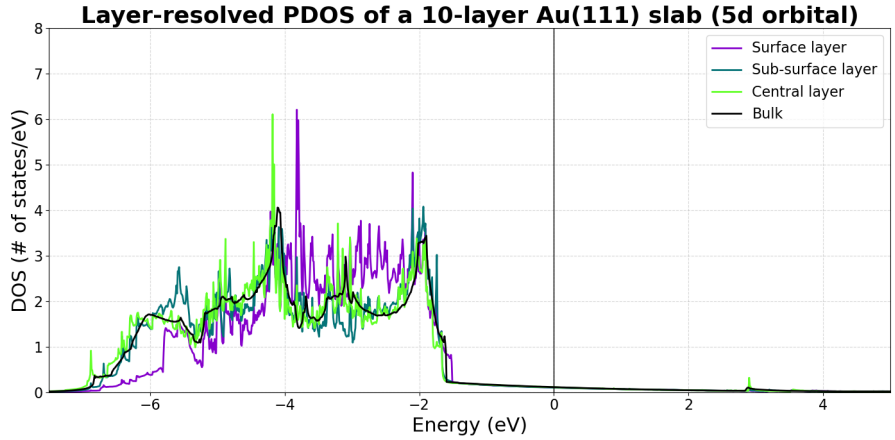

Figure 2.33: Layer-resolved PDOS of 5d orbitals of the 10-layer Au(111) slab. The bulk PDOS of the 5d orbital is added as a reference(black line). The Fermi energy is set to zero for all plots (gray vertical line).

The surface-layer PDOS of the 2-layer slab fails to reproduce the bulk profile, as it exhibits pronounced sharp features and the prominent structures are shifted towards the Fermi level. With the layer-resolved PDOS profiles for the 5-layer slab, a layer-dependent convergence to the bulk profile starts to appear: even though additional peaks are present, the central layer and the sub-surface layer start to approximate the bulk PDOS diagram, whereas the surface-layer PDOS maintains its distinct characteristics. The central-layer profile of the 10-layer slab is in good qualitative agreement with the bulk profile and the sub-surface layer also tends to bulk behaviour. This suggests to

adopt the 5-layer slab as the minimal model of the gold surface where light-activated adatom formation occurs, so as to balance accuracy and computational viability.

2.2.3 Optical properties of the Au(111) surface

Optical absorption of the Au(111) surface is studied in the long-wavelength limit, with incoming radiation oscillating with frequency ω and characterized by a small wavevector $\mathbf{q}$ ($\mathbf{q} \to 0$ limit), by calculating the optical absorption spectra of the 2-layer, 5-layer and 10-layer Au(111) slabs within the random phase approximation. Conversely to what is observed in bulk gold, the orientation of the wavevector $\mathbf{q}$ influences the results of optical-properties calculations for Au slabs, as the inclusion of vacuum breaks the symmetry of the FCC lattice. The absorption spectra are calculated for incoming wavector parallel to the x axis, and thus to the (111) surface plane, and parallel to the z axis, thus perpendicular to the surface. The computational parameters defined in Section 2.1.3 are employed; the k-point grid in the non self-consistent calculations to generate the YAMBO databases is now set to $47 \times 47 \times 1$ for the three slabs.

Initially, $\mathbf{q}$ is taken to be parallel to the surface and the imaginary part of the dielectric function is computed both neglecting and including local field effects. The absorption spectra for the three selected slabs at the independent-particle level in this configuration are presented in Fig.(2.34); the bulk spectrum at the IP level is reported in gray for comparison.

The absorption spectra with LFE are reported in Fig.(2.35) and the corresponding bulk spectrum is added as a reference. Comparison between Fig.(2.34) and Fig.(2.35) shows that, analogously to what is observed in bulk gold, there is little influence of local fields on the optical absorption spectra of the selected slabs for wavector $\mathbf{q}$ parallel to the x axis, as the slab is periodic in this direction. Both at the IP level and with the inclusion of LFE, above 1.8 eV, the absorption spectra of the selected Au(111) slabs are quenched compared to the bulk, but reproduce its overall behaviour for what concerns the absorption edge and the main peaks.

As slab thickness increases, the curves get progressively closer to the bulk profile, as expected. However, the bulk profile in the energy range between 0 and 1.8 eV is better reproduced by the 2-layer Au(111) slab; the 5-layer and 10-layer profiles show prominent peaks that become more pronounced and are shifted towards 0 eV as slab thickness is increased.

Similar structures have also been reported in Ref.[44] for 6-layer, 14-layer and 30-layer Au(111) thin films. Their origin is linked to thickness-induced changes in the electronic structure of the slab. In particular, the band structure of the thin films displays a shift of relative position of the top of the d-band at the X point, with respect to the bulk-system value; this shift depends on the film thickness. Moreover, the p-band intersects the Fermi-level for the thin films, conversely to what is observed in the bulk system. The electronic transitions between the d-band and the p-band states lead to the interband

peaks shifting with slab thickness at low energies as shown in the band structure for the 14-layer and 30-layer Au(111) thin films, taken from Ref.[44] and presented in Fig.(2.36).

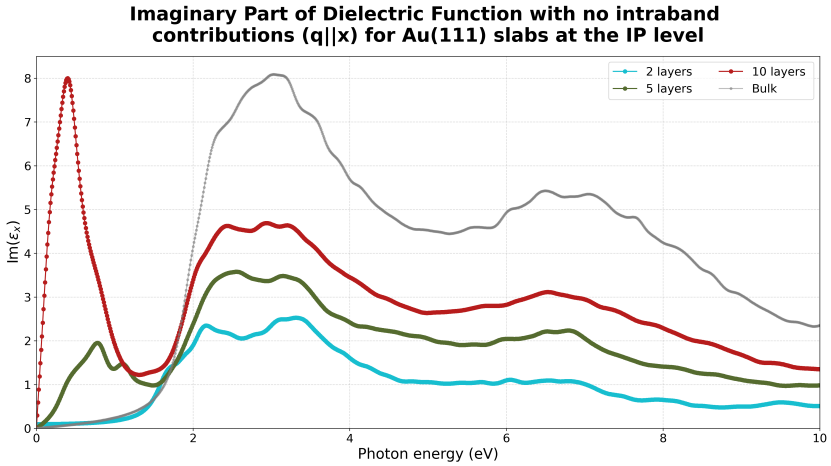

Figure 2.34: Absorption spectra for the Au(111) slabs including 2 atomic layers (light blue line), 5 atomic layers (green line), 10 atomic layers (red line), at the independent-particle level for incoming wavevector **q** parallel to the surface. The bulk spectrum at the IP-RPA level (gray line) is reported for comparison.

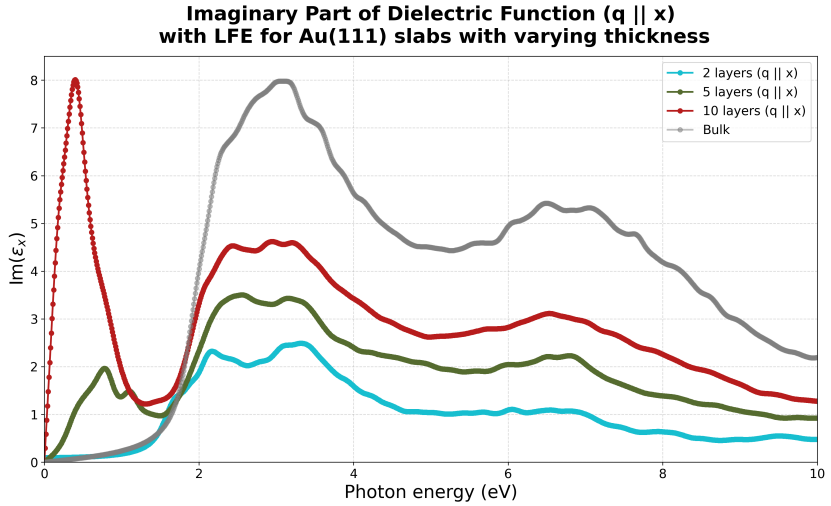

Figure 2.35: Absorption spectra for the Au(111) slabs including 2 atomic layers (light blue line), 5 atomic layers (green line), 10 atomic layers (red line), with local field effects for incoming wavevector **q** parallel to the surface. The bulk spectrum at the LFE-RPA level (gray line) is reported for comparison.

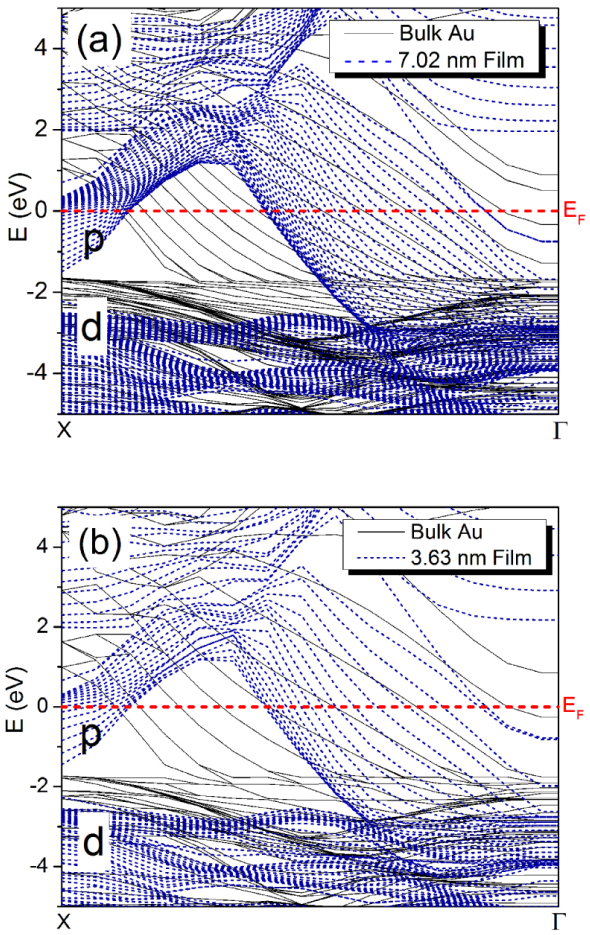

Figure 2.36: Band structure for (a) 7.02 nm, 30-layer thick and (b) 3.63 nm, 14 (111) gold thin-films in the Γ-X direction (blue dotted lines). The bulk band structure is reported as a reference (black continuous lines). Image source: Slimane Laref, Jiangrong Cao, Abu Asaduzzaman, Keith Runge, Pierre Deymier, Richard W. Ziolkowski, Mamoru Miyawaki, and Krishna Muralidharan, "Size-dependent permittivity and intrinsic optical anisotropy of nanometric gold thin films: a density functional theory study," (2013) *Opt. Express* 21, 11827-11838.

Subsequentially, the wavevector **q** is chosen to be perpendicular to the surface and equivalent calculations of the imaginary part of the dielectric function are performed. The absorption spectra for the three selected slabs at the independent-particle level are presented in Fig.(2.37), while the spectra with LFE are reported in Fig.(2.38). The corresponding bulk spectra are reported in gray for comparison in both figures. As expected, local field effects completely quench the response of the system. This is due to the depolarization field that is built within the slab as it polarizes along the z direction, under the influence of the applied field.

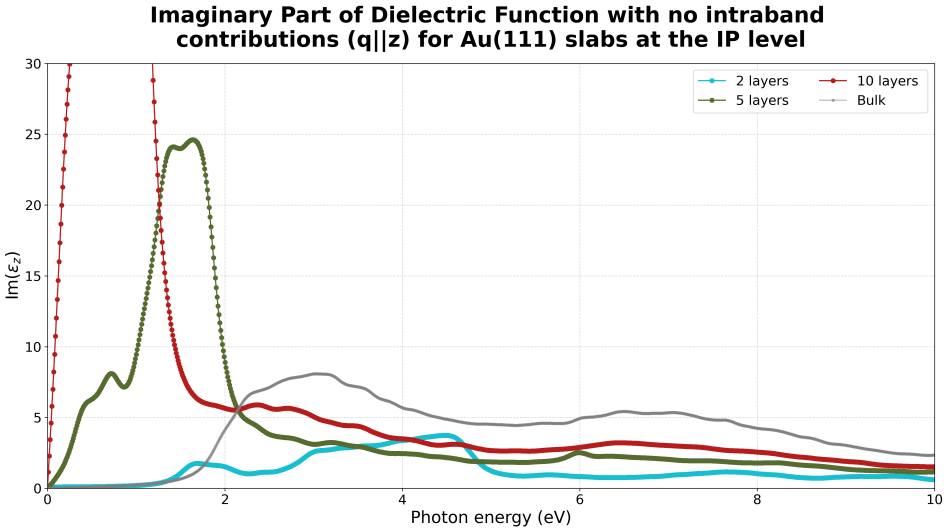

Figure 2.37: Absorption spectra for the Au(111) slabs including 2 atomic layers (light blue line), 5 atomic layers (green line), 10 atomic layers (red line), at the independent-particle level for incoming wavevector **q** normal to the surface. The bulk spectrum at the IP-RPA level (gray line) is reported for comparison.

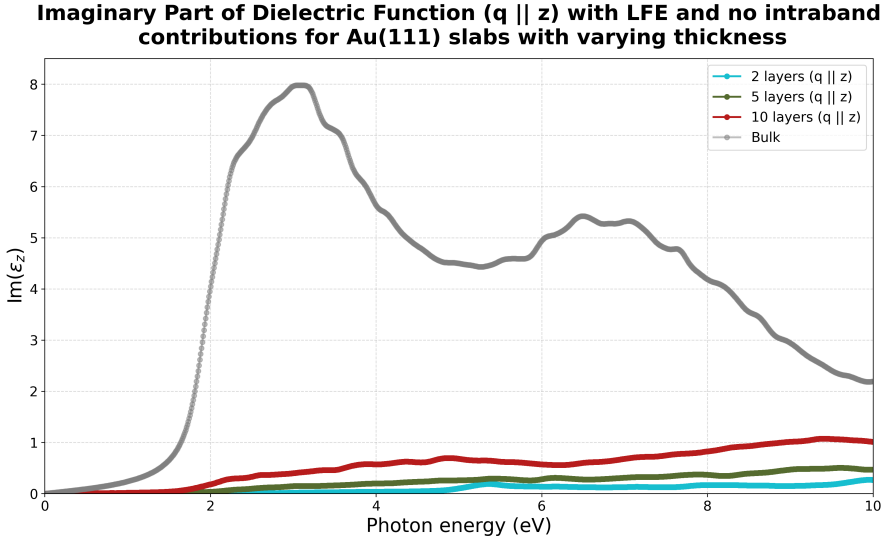

Figure 2.38: Absorption spectra for the Au(111) slabs including 2 atomic layers (light blue line), 5 atomic layers (green line), 10 atomic layers (red line), with local field effects for incoming wavevector **q** normal to the surface. The bulk spectrum at the LFE-RPA level (gray line) is reported for comparison.

Chapter 3

Conclusions

The aim of this thesis is to contribute to the identification of the minimal system required to study through DFT simulations the formation of individual adatoms from a gold facet, with molecules in its vicinity, triggered by light irradiation. This is accomplished by performing DFT electronic-structure and optical-properties calculations of bulk gold and of the Au(111) surface -through slabs of different thickness- in the GGA formalism.

Initially, the optimal computational parameters are determined through bulk calculations and convergence tests. The optimal cut-off energy, energy convergence threshold and k-point grids are identified. The optimal equilibrium lattice parameter for gold is found, both in the scalar-relativistic regime (a_{eq} =4.1518 Å) and in the fully-relativistic regime (a_{eq}=4.1457 Å); these values slightly overestimate the experimental value at room temperature. The bulk band structure, DOS and PDOS are computed in the scalar-relativistic and fully-relativistic regimes; in general, the results are consistent with literature and previous studies. Furthermore, the calculated absorption spectra for bulk Au within the RPA, both neglecting and including LFE, behave consistently with expectations.

Moving from the bulk to the Au(111) surface, the DOS of Au(111) slabs of different thickness is evaluated; the layer-resolved PDOS on the 5d orbitals is then computed for a 2-layer, a 5-layer and a 10-layer slab and compared with the corresponding bulk PDOS diagram. The comparative analysis of the layer-resolved PDOS profiles shows that the central and sub-surface layers of the 5-layer slab start to approximate bulk behaviour: the 5-layer Au(111) slab might thus be employed as the minimal model of the gold facet where light-activated adatom formation occurs. The calculated absorption spectra in the RPA for the 2-layer, 5-layer and 10-layer slabs in the direction parallel to the surface show a clear tendency to converge to the corresponding bulk spectra above the interband energy threshold, but show peaks below this threshold that become more pronounced and are shifted towards 0 eV as slab thickness is increased.

A complete characterization of the system of interest requires further investigations. To accurately model the optical properties of metals, the inclusion of intraband con-

tributions is necessary; moreover, a deeper analysis is required to precisely understand the physical nature of the peaks observed in the slab absorption spectra. Many-body effects beyond mean-field DFT should also be assessed and tested against slab thickness. Finally, future studies should investigate how the electronic structure and optical properties are modified by the presence of adatoms on the surface, in order to lay the foundation for accurate simulations of gold nanoparticle-on-mirror systems, enclosing a self-assembled monolayer, where light-activated adatom formation occurs.

Ringraziamenti

Desidero innanzitutto ringraziare la professoressa Margherita Marsili per avermi accompagnata nella stesura di questa tesi. La competenza e l'attenzione fuori dal comune con cui ha guidato il mio processo di apprendimento mi hanno permesso di espandere le mie conoscenze più di quanto avrei potuto immaginare e la fiducia che ha riposto nelle mie capacità mi è preziosa.

Voglio esprimere poi la mia gratitudine verso la mia famiglia, vasta, complicata e bellissima, sempre pronta a incoraggiarmi. Un ringraziamento speciale va ai miei genitori, Marco e Cristina, che mi hanno permesso di intraprendere questo percorso universitario e che da tutta la vita mi regalano il loro amore e il loro sostegno incondizionato. A mia sorella Giulia devo i ringraziamenti più sentiti; nonostante tutte le nostre differenze e la distanza geografica che ci separa, ormai da molti anni, rimane sempre la mia prima complice e il mio punto di riferimento. Anche i miei nonni, Tina e Basilio, meritano una menzione d'onore per non aver mai mancato di dimostrarmi la loro stima e di colmarmi d'affetto.

Voglio quindi ringraziare la moltitudine di amiche e di amici che negli anni ha visto e accolto le più disparate versioni di me, anche le più difficili. Spero di poter restituire a ognuno di loro tutta la gioia con cui hanno illuminato le mie giornate.

Infine voglio ringraziare Luca, che da quando mi conosce non ha mai smesso di tifare per me e, quando ne avevo più bisogno, ha saputo ricordarmi il mio valore.

Bibliography

[1] Qianqi Lin et al. "Optical suppression of energy barriers in single molecule-metal binding". In: *Science Advances* 8.25 (2022), eabp9285. DOI: 10.1126/sciadv.abp9285. eprint: https://www.science.org/doi/pdf/10.1126/sciadv.abp9285. URL: https://www.science.org/doi/abs/10.1126/sciadv.abp9285.

[2] G. Grosso and G.P. Parravicini. *Solid State Physics*. Academic Press, 2000. ISBN: 9780080481029. URL: https://books.google.it/books?id=L5RrQbbvWn8C.

[3] Eite Tiesinga et al. *The 2022 CODATA Recommended Values of the Fundamental Physical Constants*. Web Version 9.0. Database developed by J. Baker, M. Douma, and S. Kotochigova. National Institute of Standards and Technology. 2024. URL: https://physics.nist.gov/constants.

[4] Richard M. Martin. *Electronic Structure: Basic Theory and Practical Methods*. Cambridge University Press, 2004.

[5] N. W. Ashcroft and N. D. Mermin. *Solid State Physics*. Holt-Saunders, 1976.

[6] Kieron Burke. "Perspective on Density Functional Theory". In: *The Journal of chemical physics* 136 (Apr. 2012), p. 150901. DOI: 10.1063/1.4704546.

[7] Klaus Capelle. *A bird's-eye view of density-functional theory*. 2006. arXiv: cond-mat/0211443 [cond-mat.mtrl-sci]. URL: https://arxiv.org/abs/cond-mat/0211443.

[8] P. Hohenberg and W. Kohn. "Inhomogeneous Electron Gas". In: *Phys. Rev.* 136 (3B Nov. 1964), B864–B871. DOI: 10.1103/PhysRev.136.B864. URL: https://link.aps.org/doi/10.1103/PhysRev.136.B864.

[9] W. Kohn and L. J. Sham. "Self-Consistent Equations Including Exchange and Correlation Effects". In: *Phys. Rev.* 140 (4A Nov. 1965), A1133–A1138. DOI: 10.1103/PhysRev.140.A1133. URL: https://link.aps.org/doi/10.1103/PhysRev.140.A1133.

[10] John P. Perdew, Kieron Burke, and Matthias Ernzerhof. "Generalized Gradient Approximation Made Simple". In: *Phys. Rev. Lett.* 77 (18 Oct. 1996), pp. 3865–3868. DOI: 10.1103/PhysRevLett.77.3865. URL: https://link.aps.org/doi/10.1103/PhysRevLett.77.3865.

[11] David S. Sholl and Janice A. Steckel. *Nuts and Bolts of DFT Calculations*. John Wiley and Sons, Ltd, 2009. ISBN: 9780470447710. DOI: https://doi.org/10.1002/9780470447710.ch3. eprint: https://onlinelibrary.wiley.com/doi/pdf/10.1002/9780470447710.ch3. URL: https://onlinelibrary.wiley.com/doi/abs/10.1002/9780470447710.ch3.

[12] G. Lehmann and M. Taut. "On the Numerical Calculation of the Density of States and Related Properties". In: *physica status solidi (b)* 54.2 (1972), pp. 469–477. DOI: https://doi.org/10.1002/pssb.2220540211. eprint: https://onlinelibrary.wiley.com/doi/pdf/10.1002/pssb.2220540211. URL: https://onlinelibrary.wiley.com/doi/abs/10.1002/pssb.2220540211.

[13] D. R. Hamann, M. Schlüter, and C. Chiang. "Norm-Conserving Pseudopotentials". In: *Phys. Rev. Lett.* 43 (20 Nov. 1979), pp. 1494–1497. DOI: 10.1103/PhysRevLett.43.1494. URL: https://link.aps.org/doi/10.1103/PhysRevLett.43.1494.

[14] Leonard Kleinman. "Relativistic norm-conserving pseudopotential". In: *Phys. Rev. B* 21 (6 Mar. 1980), pp. 2630–2631. DOI: 10.1103/PhysRevB.21.2630. URL: https://link.aps.org/doi/10.1103/PhysRevB.21.2630.

[15] Erich Runge and E. K. U. Gross. "Density-Functional Theory for Time-Dependent Systems". In: *Phys. Rev. Lett.* 52 (12 Mar. 1984), pp. 997–1000. DOI: 10.1103/PhysRevLett.52.997. URL: https://link.aps.org/doi/10.1103/PhysRevLett.52.997.

[16] C. Ullrich. *Time-Dependent Density-Functional Theory: Concepts and Applications*. Oxford Graduate Texts. OUP Oxford, 2012. ISBN: 9780199563029. URL: https://books.google.it/books?id=hCNNsC4sEtkC.

[17] Silvana Botti. "Semi-empirical and ab initio calculations of the optical properties of semiconductor superlattices". Theses. Università degli studi di Pavia, Feb. 2002. URL: https://theses.hal.science/tel-00520076.

[18] Paolo Giannozzi et al. "QUANTUM ESPRESSO: a modular and open-source software project for quantum simulations of materials". In: *Journal of Physics: Condensed Matter* 21.39 (2009), p. 395502. ISSN: 1361-648X. DOI: 10.1088/0953-8984/21/39/395502. URL: http://dx.doi.org/10.1088/0953-8984/21/39/395502.

[19] P Giannozzi et al. "Advanced capabilities for materials modelling with Quantum ESPRESSO". In: *Journal of Physics: Condensed Matter* 29.46 (Oct. 2017), p. 465901. ISSN: 1361-648X. DOI: 10.1088/1361-648x/aa8f79. URL: http://dx.doi.org/10.1088/1361-648X/aa8f79.

[20] Andrea Marini et al. "yambo: An ab initio tool for excited state calculations". In: *Computer Physics Communications* 180.8 (2009), pp. 1392–1403. ISSN: 0010-4655. DOI: https://doi.org/10.1016/j.cpc.2009.02.003. URL: https://www.sciencedirect.com/science/article/pii/S0010465509000472.

[21] D Sangalli et al. "Many-body perturbation theory calculations using the yambo code". In: *Journal of Physics: Condensed Matter* 31.32 (May 2019), p. 325902. DOI: 10.1088/1361-648X/ab15d0. URL: https://doi.org/10.1088/1361-648X/ab15d0.

[22] D. R. Hamann. "Optimized norm-conserving Vanderbilt pseudopotentials". In: *Phys. Rev. B* 88 (8 Aug. 2013), p. 085117. DOI: 10.1103/PhysRevB.88.085117. URL: https://link.aps.org/doi/10.1103/PhysRevB.88.085117.

[23] United States. National Bureau of Standards and H.E. Swanson. *Standard X-ray Diffraction Powder Patterns*. (National Bureau of Standards Circular 539, Volume I). U.S. Department of Commerce, National Bureau of Standards, 1953.

[24] Chang Liu et al. "Exceptional strain strengthening and tuning of mechanical properties of TiN". In: *Phys. Rev. B* 106 (5 Aug. 2022), p. 054112. DOI: 10.1103/PhysRevB.106.054112. URL: https://link.aps.org/doi/10.1103/PhysRevB.106.054112.

[25] AFLOW Automatic-FLOW for Materials Discovery. *Au (ICSD 64701, AUID aflow:91f4eefd3b15e44d)*. URL: https://aflow.org/material/?id=aflow:91f4eefd3b15e44d.

[26] Stefano Curtarolo et al. "AFLOW: An automatic framework for high-throughput materials discovery". In: *Computational Materials Science* 58 (2012), pp. 218–226. DOI: 10.1016/j.commatsci.2012.02.005.

[27] N. Egede Christensen and B. O. Seraphin. "Relativistic Band Calculation and the Optical Properties of Gold". In: *Phys. Rev. B* 4 (10 Nov. 1971), pp. 3321–3344. DOI: 10.1103/PhysRevB.4.3321. URL: https://link.aps.org/doi/10.1103/PhysRevB.4.3321.

[28] M. Y. Toriyama et al. *Comparison of the Tetrahedron Method to Smearing Methods for the Electronic Density of States*. 2021. arXiv: 2103.03469 [cond-mat.mtrl-sci]. URL: https://arxiv.org/abs/2103.03469.

[29] Ewen Lallinec and Antoine Levitt. *Numerical methods for the computation of densities of states of periodic operators*. 2026. arXiv: 2603.29457 [math.NA]. URL: https://arxiv.org/abs/2603.29457.

[30] J Aarons et al. "Atom-projected and angular momentum resolved density of states in the ONETEP code". In: *Electronic Structure* 1.3 (Aug. 2019), p. 035002. DOI: 10.1088/2516-1075/ab34f5. URL: https://doi.org/10.1088/2516-1075/ab34f5.

[31] Robert Martin Eisberg and Robert Resnick. *Quantum Physics of Atoms, Molecules, Solids, Nuclei, and Particles*. 2nd. New York, NY: John Wiley & Sons, 1985. ISBN: 978-0471873730.

[32] Michael R. Beversluis, Alexandre Bouhelier, and Lukas Novotny. "Continuum generation from single gold nanostructures through near-field mediated intraband transitions". In: *Phys. Rev. B* 68 (11 Sept. 2003), p. 115433. DOI: 10.1103/PhysRevB.68.115433. URL: https://link.aps.org/doi/10.1103/PhysRevB.68.115433.

[33] T. Rangel et al. "Band structure of gold from many-body perturbation theory". In: *Phys. Rev. B* 86 (12 Sept. 2012), p. 125125. DOI: 10.1103/PhysRevB.86.125125. URL: https://link.aps.org/doi/10.1103/PhysRevB.86.125125.

[34] Krystyna Kolwas and Anastasiya Derkachova. "Impact of the Interband Transitions in Gold and Silver on the Dynamics of Propagating and Localized Surface Plasmons". In: *Nanomaterials* 10.7 (2020). ISSN: 2079-4991. DOI: 10.3390/nano10071411. URL: https://www.mdpi.com/2079-4991/10/7/1411.

[35] Pekka Pyykko and Jean Paul Desclaux. "Relativity and the periodic system of elements". In: *Accounts of Chemical Research* 12.8 (1979), pp. 276–281. DOI: 10.1021/ar50140a002. eprint: https://doi.org/10.1021/ar50140a002. URL: https://doi.org/10.1021/ar50140a002.

[36] Dario A. Leon et al. "Efficient full frequency GW for metals using a multipole approach for the dielectric screening". In: *Phys. Rev. B* 107 (15 Apr. 2023), p. 155130. DOI: 10.1103/PhysRevB.107.155130. URL: https://link.aps.org/doi/10.1103/PhysRevB.107.155130.

[37] Robert L. Olmon et al. "Optical dielectric function of gold". In: *Phys. Rev. B* 86 (23 Dec. 2012), p. 235147. DOI: 10.1103/PhysRevB.86.235147. URL: https://link.aps.org/doi/10.1103/PhysRevB.86.235147.

[38] P. B. Johnson and R. W. Christy. "Optical Constants of the Noble Metals". In: *Phys. Rev. B* 6 (12 Dec. 1972), pp. 4370–4379. DOI: 10.1103/PhysRevB.6.4370. URL: https://link.aps.org/doi/10.1103/PhysRevB.6.4370.

[39] Maria K Pogodaeva et al. "Dielectric function of six elemental metals". In: *Journal of Physics: Conference Series* 1890.1 (Apr. 2021), p. 012008. DOI: 10.1088/1742-6596/1890/1/012008. URL: https://doi.org/10.1088/1742-6596/1890/1/012008.

[40] Ask Hjorth Larsen et al. "The atomic simulation environment—a Python library for working with atoms". In: *Journal of Physics: Condensed Matter* 29.27 (June 2017), p. 273002. DOI: 10.1088/1361-648X/aa680e. URL: https://doi.org/10.1088/1361-648X/aa680e.

[41] Wenhao Sun and Gerbrand Ceder. "Efficient creation and convergence of surface slabs". In: *Surface Science* 617 (2013), pp. 53–59. ISSN: 0039-6028. DOI: https://doi.org/10.1016/j.susc.2013.05.016. URL: https://www.sciencedirect.com/science/article/pii/S003960281300160X.

[42] Vincenzo Fiorentini and M Methfessel. “Extracting convergent surface energies from slab calculations”. In: *Journal of Physics: Condensed Matter* 8.36 (Sept. 1996), p. 6525. DOI: 10.1088/0953-8984/8/36/005. URL: https://doi.org/10.1088/0953-8984/8/36/005.

[43] Paul Harrison and Alexander Valavanis. *Quantum Wells, Wires and Dots: Theoretical and Computational Physics of Semiconductor Nanostructures*. John Wiley and Sons, Apr. 2016. ISBN: 9781118923368. DOI: 10.1002/9781118923337.

[44] Slimane Laref et al. “Size-dependent permittivity and intrinsic optical anisotropy of nanometric gold thin films: a density functional theory study”. In: *Opt. Express* 21.10 (May 2013), pp. 11827–11838. DOI: 10.1364/OE.21.011827. URL: https://opg.optica.org/oe/abstract.cfm?URI=oe-21-10-11827.